Available online at www.sciencedirect.com
ScienceDirect
Coordination Chemistry Reviews 252 (2008) 1007–1026
COORDINATION CHEMISTRY REVIEWS
www.elsevier.com/locate/ccr

Review

Syntheses and functions of porous metallosupramolecular networks

Myunghyun Paik Suh*, Young Eun Cheon, Eun Young Lee

Department of Chemistry, Seoul National University, San 56-1, Sillim-dong, Kwanak-gu, Seoul 151-747, Republic of Korea

Received 17 September 2007; accepted 28 January 2008
Available online 7 February 2008

Contents

Abstract

Design and synthetic strategies for the construction of porous metallosupramolecular networks are presented. The porous metallosupramolecular networks show various functions such as gas adsorption, molecular recognition, ion exchange, sensing, and production of metal nanoparticles. Their specificities depend on the pore shape, size, and chemical environments of the voids or channels. In this review, relationship between the structures and functions is discussed.

Keywords: Metallosupramolecular networks; Metal-organic frameworks; Coordination polymers; Gas storage; Gas separation; Guest binding; Sensors; Macrocyclic complexes; Secondary building units; Self-assembly; Solvothermal reactions; Selectivity

1. Introduction

'*Supramolecular chemistry*' was defined by Jean-Marie Lehn as '*the chemistry of molecular assemblies and of intermolecular bonds*' and was discriminated from 'molecular chemistry' based on the covalent bond [1,2]. Supramolecules bear the organized entities of higher complexity that result from the association of two or more chemical species held together by intermolecular forces [1,2]. Supramolecules are formed by the intermolecular interactions such as hydrogen bonds [3–5], π–π interactions [6], van der Waals interactions, cation–π interactions [7], and metal–ligand coordination bonds [8,9]. To achieve a designed supramolecular assembly, appropriate combination of properly designed molecular building units should be made, which is referred to 'crystal engineering' [10].

Metallosupramolecules are constructed mainly by coordination bonds between metal ions and ligands, together with other intermolecular interactions. The goals for construction of metal-

* Corresponding author. Tel.: +82 2 880 7760; fax: +82 2 886 8516.
E-mail address: mpsuh@snu.ac.kr (M.P. Suh).

0010-8545/$ – see front matter © 2008 Elsevier B.V. All rights reserved.
doi:10.1016/j.ccr.2008.01.032

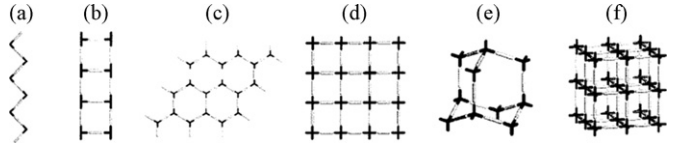

Fig. 1. Schematic representations of some of the simple network architectures. (a) 1D zigzag chain, (b) 1D ladder, (c) 2D honeycomb, (d) 2D square grid, (e) 3D hexagonal diamondoid, and (f) 3D cubic framework. Reproduced with permission from Ref. [9].

losupramolecular networks are to obtain the materials that show specific or multifunctional properties. Among various metallosupramolecular networks, porous networks that contain empty space where guest molecules are occupied are of particular interest because they have great potentials to be applied in molecular adsorption and separation processes [11–17], ion exchange [18–20], catalysis [21–23], sensor technology [24–26], and opto-electronics [27].

2. Assembly of porous metallosupramolecular networks

The simple architectures of the networks assembled from metal ions and organic ligands are presented in Fig. 1, which can be easily imagined by intuition just like playing with the *Lego* blocks.

More complicated 3D structures can be achieved by mimicking the topologies of the conventional inorganic solids (Fig. 2) [28,29]. This approach has been based on the idea of nets, which are the abstract mathematical entities consisting of a collection of points or nodes with defined connectivity [30].

For description of the topology of the ordered networks, Yaghi and co-workers have suggested relatively easy expressions [28]. When all vertices are linked to *N* neighbors, the topology is called as a *N*-connected net. When some vertices are connected to *N* neighbors and some to *M* neighbors, it is named as a (*N*,*M*)-connected net. In Fig. 2(a) and (b) belong to 3-connected nets, (c) and (d) belong to (3,4)-connected nets, (e) belongs to a (3,6)-connected net, (f), (g), and (h) belong to 4-connected nets, (i) belongs to a (4,6)-connected net, (j) belongs to a (4,8)–connected net, (k) and (l) belong to a 6-connected net, and a 8-connected net, respectively.

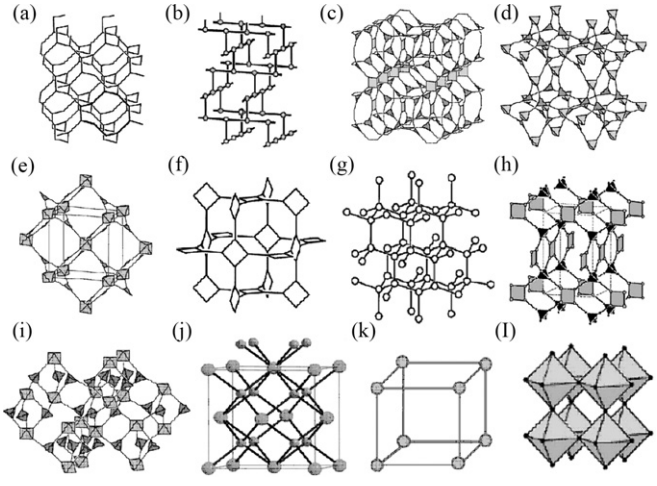

Fig. 2. (a) $SrSi_2$ net, (b) $ThSi_2$ net, (c) Pt_3O_4 net, (d) boracite net, (e) rutile (TiO_2) net, (f) NbO net, (g) diamondoid net, (h) cooperate (PtS) net, (i) corundum (Al_2O_3) net, (j) fluorite (CaF_2) net, (k) primitive cubic, and (l) body centered cubic net. Reproduced with permission from Ref. [29].

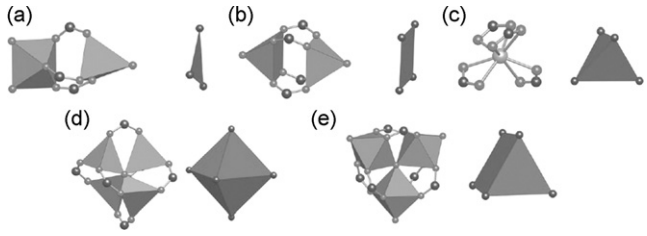

Fig. 3. Examples of inorganic SBUs. (a) Triangle, (b) square planar, (c) tetrahedron, (d) octahedron, and (e) trigonal prism. Reproduced with permission from Ref. [31].

2.1. Solvothermal synthesis and structures

It is difficult to predict the network structures produced from the solvothermal reactions of simple metal ion and organic linkers, because free metal ions contain too many binding sites for the organic linkers and have little directional information. Yaghi et al. defined the secondary building unit (SBU) as '*geometry of the unit defined by the point of extension*' and illustrated the possible inorganic SBUs (Fig. 3). The design and synthesis of metallosupramolecular networks based on SBUs facilitate network design and synthesis [31].

A series of networks with wide ranges of pore size has been assembled from Zn(II) ion and various dicarboxylate linkers under closely related, not identical, conditions (Fig. 4). In these networks, a μ_4-oxo bridged Zn_4O tetrahedron cluster that is edge-bridged by six carboxylate groups of dicarboxylates provides the octahedron shaped SBU. The $Zn_4O(CO_2)_6$ SBUs locate at the nodes and the organic parts reside as the struts of the cube. The frameworks with bigger cavities or channels can be synthesized by employing longer building blocks [32].

In the solvothermal reaction of metal and organic building blocks, various reaction conditions such as type of metal ions, type of organic building blocks, temperature, solvent, and the

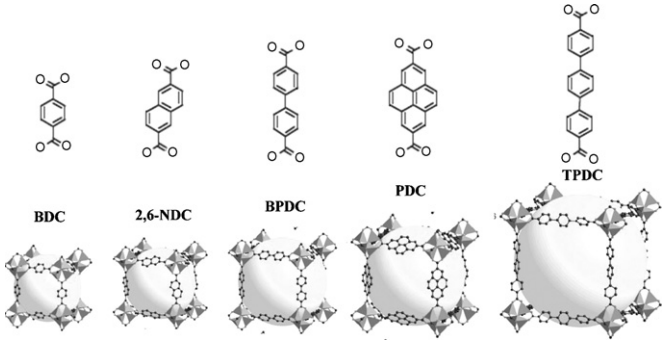

Fig. 4. Single crystal X-ray structures assembled from Zn(II) with BDC^{2-} (1,4,-benzenedicarboxylate), 2,6-NDC^{2-} (2,6-naphthalenedicarboxylate), $BPDC^{2-}$ (biphenyldicarboxylate), PDC^{2-} (pyrenedicarboxylate), and $TPDC^{2-}$ (triphenyldicarboxylate), respectively. Reproduced with permission from Ref. [32].

rate of crystallization affect the topology of porous networks. For example, when the metal ion is changed from Zn(II) to Mn(II) in the synthesis, different framework is formed even though the same dicarboxylate is employed as the organic building block [32,33].

A 3D network, $[Mn(NDC)(DEF)]_n$ (**1**-**1**) where NDC is 2,6-naphthalenedicarboxylate and DEF is *N*,*N*′-diethylformamide, was prepared from the solvothermal reaction of $Mn(NO_3)_2{\cdot}nH_2O$ and H_2NDC at 105 °C in DEF [33]. In **1**-**1**, each Mn(II) is coordinated with six oxygen atoms that belong to four carboxylato groups and one DEF, showing pseudo-octahedral coordination geometry. The Mn(II) ions are bridged by carboxylato groups to form a 1D Mn(II) chain. The 1D Mn(II) chains are linked with one to the other via naphthalene rings of NDC^{2-} to form a 3D network that generates 1D channels of rhombic aperture with diagonal lengths of 21.5 Å × 10.5 Å (Fig. 5). The effective window size of the channels is ca. 6.1 Å. The network has no free space because the DEF molecules coordinating Mn(II) ions occupy the channels. However, when DEF molecules coordinating Mn(II) ions are removed by heating the solid at 250 °C under vacuum for 18 h, structural change occurs as evidenced by X-ray powder diffraction patterns. Desolvated solid $[Mn(NDC)]_n$ (**1**-**1**′) contains coordinatively unsaturated Mn(II) sites, as evidenced by elemental analysis, IR, TGA, and XRPD data.

The 3D frameworks constructed from NDC^{2-} and other metal ions such as Mg^{2+} and Ni^{2+} show different structures from either of **1**-**1** or any of Fig. 4 [34,35].

Porous metallosupramolecular networks have been prepared by using the metal ions and tricarboxylate NTB^{3-} (H_3NTB = 4,4′,4″-nitrilotrisbenzoic acid) as the organic building block [36,37]. Suh's group prepared a porous network $[Zn_4O(NTB)_2]_n{\cdot}3n$DEF·*n*EtOH (**1**-**2**) by using $Zn(NO_3)_2{\cdot}6H_2O$ and H_3NTB in DEF, EtOH, and H_2O mixture [36]. In **1**-**2**, $Zn_4O(CO_2)_6$ octahedral SBUs are linked by the NTB^{3-} units to form PdF_2 type (3,6)-connected nets, which are doubly interpenetrated to generate curved 3D channels (Fig. 6). The network exhibits multi-functionalities, as described in Sections 3.1, 4, and 6. Most interestingly, the single crystallinity was retained even when **1**-**2** was heated at 400 °C and 10^{-5} Torr to remove all guest solvent molecules. X-ray single crystal structure exhibited that the molecular components in the crystal performed reversible dynamic motions, mainly the rotational motions, in response to removal and rebinding of the guest molecules [36]. To retain the single crystal integrity, extensive cooperative motions between the molecular components should occur throughout the crystal.

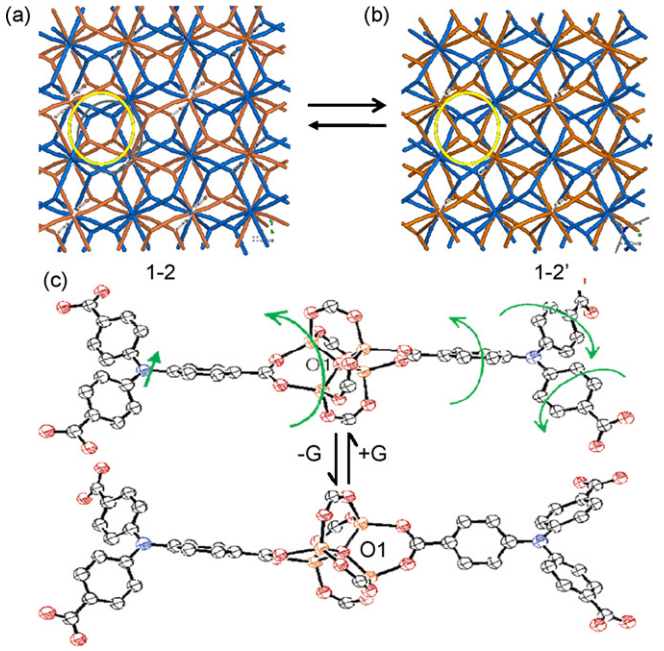

Fig. 6. (a) Doubly interpenetrated PdF_2 type network of $[Zn_4O(NTB)_2]_n{\cdot}3n$DEF·*n*EtOH (**1**-**2**) and (b) $[Zn_4O(NTB)_2]_n$ (**1**-**2**′). (c) Rearrangements of the framework components upon guest removal and rebinding. Thermal ellipsoids are drawn with 50% probability. Color scheme: Zn, yellow; O, red; N, blue; C, gray. Reproduced with permission from Ref. [36].

When similar solvothermal synthesis was carried out at 110 °C in EtOH, the different solvent system from **1**-**2**, the 3D network $[Zn_3(NTB)_2(EtOH)_2]_n{\cdot}4n$EtOH (**1**-**3**) was produced, which generated 1D channels of honeycomb aperture [37]. The structure of **1**-**3** consisted of Zn_3 cluster unit, where two terminal Zn atoms are in the distorted trigonal bipyramidal (tbp) coordination geometry by binding an EtOH molecule at the axial site, with the central Zn atom in the tetrahedral coordination geometry. Interestingly, it was revealed by the single crystal X-ray analysis that on removal and rebinding of the coordinating EtOH molecule, the coordination geometry of Zn(II) transformed reversibly from/to trigonal bipyramid to/from tetrahedron, together with the rotational motion of carboxylate plane of the NTB^{3-} (Fig. 7 and Scheme 1). Even after the loss of coor-

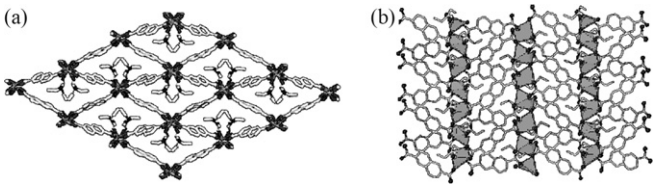

Fig. 5. (a) Top view of **1**-**1** showing a 3D network generating 1D channels that are occupied by DEF molecules coordinating Mn(II) ions. (b) Side view showing the 1D Mn(II) chains that are linked with each other via the naphthalene rings of NDC^{2-}. Reproduced with permission from Ref. [33].

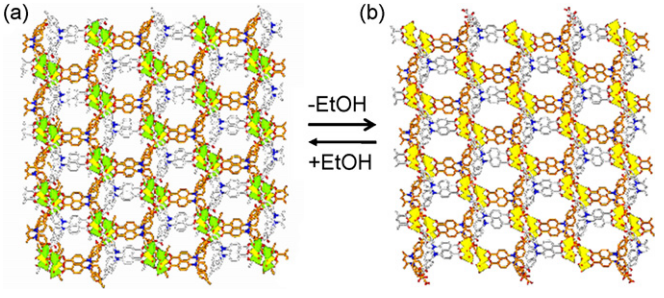

Fig. 7. X-ray crystal structures of (a) $[Zn_3(NTB)_2(EtOH)_2]_n{\cdot}4n$EtOH (**1**-**3**) and (b) $[Zn_3(NTB)_2]_n$ (**1**-**3**′). Guest EtOH molecules are omitted for clarity. Color scheme: Zn (td), yellow; Zn (tbp), green; N, blue; O, red; C of two different bilayers, white and brown. Reproduced with permission from Ref. [37].

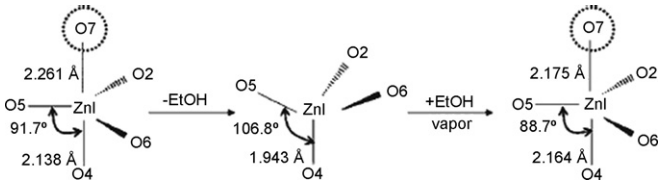

Scheme 1. Rearrangement of coordination geometry of Zn(II) ion on removal and rebinding of a coordinating EtOH molecule in **1**-**3**. Reproduced with permission from Ref. [37].

dinating EtOH as well as guest EtOH molecules, the network exhibits permanent porosity, high thermal stability, blue luminescence, and high N_2, H_2, CO_2, and CH_4 gas storage capacities as described in Section 3.1.

The metallosupramolecular networks prepared from the solvothermal reactions are often catenated. The catenation means that two or more identical networks are intergrown at the expense of pore volume. This may take the form of interpenetration where the networks are maximally displaced from each other, or interweaving where they are minimally displaced and exhibit close contacts that may result in mutual reinforcement [38]. It has been believed that (i) the use of long linkers for the design of networks with large pores results in interpenetrated structures and thus small pores, (ii) highly interpenetrated networks have low porosity (<20%), and (iii) interpenetration contributes negatively to the structural stability and porosity of networks [39]. However, there are some examples that highly interpenetrated networks provide high porosity [36,40–42].

For example, previously mentioned **1**-**2** that has doubly interpenetrated PdF_2-net structure shows high permanent porosity (Langmuir surface area, 1121 m^2/g; pore volume, 0.51 cm^3/cm^3) and high thermal stability (up to 430 °C) [36].

Yaghi and co-workers reported MOF-14, $[Cu_3(BTB)_2(H_2O)_3]\cdot(DMF)_9\cdot(H_2O)_2$ (**1**-**4**) (BTB = 4,4′,4″-benzene-1,3,5-triyl tribenzoate which has doubly interwoven structure. **1**-**4** shows exceptionally high pore volume (0.53 cm^3/g by DR equation) and large Langmuir surface area (1502 m^2/g). The interwoven pair of networks in MOF-14 occupies only a small fraction of the available space in the crystal and generates large cavities. The aperture joining two cavities has a dimension of 7.66 Å [40].

Lin et al. prepared fourfold interpenetrated 3D networks, $[Zn_4(\mu_4\text{-}O)(L_1)_3(DMF)_2]\cdot 4DMF\cdot 3CH_3OH\cdot 2H_2O$ (**1**-**5**) (L_1 = 6,6′-dichloro-2,2′-diethoxy-1,1′-binaphthyl-4,4′-dibenzoate) and $[Zn_4(\mu_4\text{-}O)(L_2)_3]\cdot 5DMF\cdot 5C_2H_5OH\cdot H_2O$ (**1**-**6**) (L_2 = 6,6′-dichloro-2,2′-dibenzyloxy-1,1′-binaphthyl-4,4′-dibenzoate). In spite of the high interpenetration, they generate 3D channels and exhibit permanent porosity (Langmuir Surface area, 502 m^2/g for **1**-**5**; 396 m^2/g for **1**-**6** by CO_2 adsorption). Powder X-ray diffraction patterns further indicated that the network structures of **1**-**5** and **1**-**6** were retained upon complete removal of the guest molecules [41].

Zhou et al. prepared $[Cu_3(TATB)_2(H_2O)_3]\cdot 3DMSO\cdot 11H_2O$ (**1**-**7**) from $Cu(NO_3)_2\cdot 2.5H_2O$ and TATB (TATB = 4,4′,4″-*s*-triazine-2,4,6-triyltribenzoate) in DMSO. The X-ray structure reveals the doubly interpenetrated (3,4)-connected Pt_3O_4-type network. On removal of coordinating water molecules as well as guest solvent molecules, coordinatively unsaturated metal sites are generated. The network exhibits permanent porosity (Langmuir surface area, 3800 m^2/g; pore volume, 1.45 mL/g by N_2 adsorption) and high hydrogen adsorption capacity (1.9 wt% at 77 K and 760 Torr) [42].

They also observed 'framework-catenation isomerism' in different solvent system. A different porous network $[Cu_6(H_2O)_6(TATB)_4]\cdot DMA\cdot 12H_2O$ (**1**-**7**′) was prepared from the same building blocks in DMA/oxalic acid. Both **1**-**7** and **1**-**7**′ have the twisted boracite-net structure that consists of $Cu_2(CO_2)_4$ paddlewheel SBUs, but **1**-**7**′ is not interpenetrated. Although oxalic acid is not involved in the net-structure of **1**-**7**′, it seems to act as the template in the formation of **1**-**7**′ [43].

2.2. Metallosupramolecular isomerism

Major problem in prediction of the network structure formed from the reaction is 'supramolecular isomerism', which includes the structural diversity and polymorphism of the network [9,44]. Metallosupramolecular network structures are greatly affected by the reaction conditions such as stoichiometry of the reactants, type of solvent, and temperature, even if same molecular building blocks are employed (Fig. 8).

Kitagawa and co-workers reported that the isomerism occurred with a fixed stoichiometry for all reaction components in the same solvent [44,45]. They studied systematically the crystallization process of $[CuI_2(\mu_2\text{-}BQ)(\mu_2\text{-}OAc)_2]$ (BQ = *p*-benzoquinone, **1**-**8**) only by varying the reaction temperature and concentration of the reactants, and obtained three different supramolecular isomers (Fig. 9). In Fig. 9(c), top, middle, and bottom lines represent XRPD patterns of the α-, β-, and γ-phases, respectively. The α-phase formed from the low temperature and high concentration is kinetically the most favored while γ-phase formed from the high temperature and low concentration is thermodynamically the most favored. The synthesis with 50 mM concentration of the building blocks at 60 °C and 30 °C results in the mixtures of two phases [45].

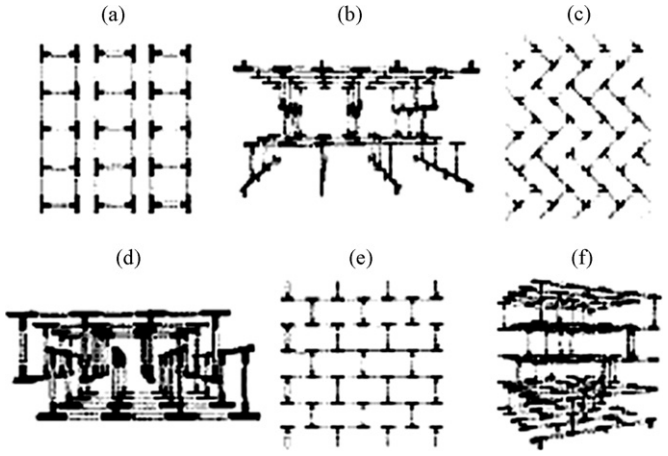

Fig. 8. Schematic illustration of the six supramolecular isomers reported for T-shaped nodes linked by linear bifunctional exodentate ligands: (a) 1D ladder, (b) 3D lincoln logs, (c) 2D herringbone, (d) 2D bilayer, (e) 2D brick wall, and (f) 3D frame. Reproduced with permission from Ref. [9].

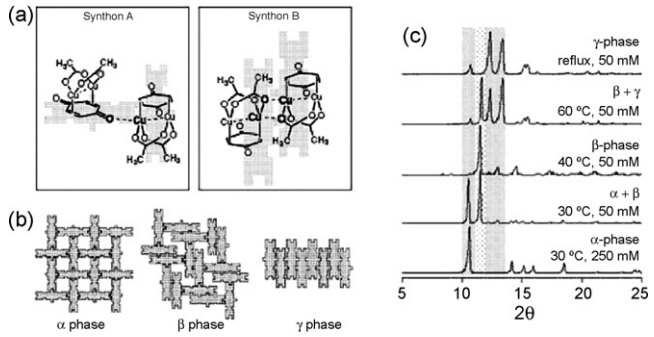

Fig. 9. (a) Two types of supramolecular synthon on coordination between two dicopper building blocks. (b) Schematic representation of three supramolecular isomers. (c) The XRPD patterns of $[CuI_2(\mu_2\text{-BQ})(\mu_2\text{-OAc})_2]$ (**1**-**8**), which depend on the reaction temperature and concentration of the reactants. Reproduced with permission from Ref. [45].

Yaghi and co-workers reported transformations between two metal-organic frameworks, $[Co_2(BPTC)(H_2O)_5]\cdot(DMF)_3(EtOH)(H_2O)_4$, (MOF-501, **1**-**9**) and $[Co_2(BPTC)(H_2O)(DMF)_2]\cdot(DMF)(H_2O)_{1.5}$, (MOF-502, **1**-**10**), which are prepared from the solvothermal reaction of $Co(NO_3)_2\cdot6H_2O$ and H_4BPTC (3,3′,5,5′-biphenyltetracarboxylic acid) in $DMF/C_2H_5OH/H_2O$. From the reaction, MOF-501 having NbO topology and small amount of MOF-502 having PtS topology were simultaneously formed, while proportion of MOF-502 is increased when the reaction time is extended. The structural transformation from MOF-501 to MOF-502 occurred when isolated MOF-501 crystals were immersed in the mother liquor and heated at 75 °C for 96 h (Fig. 10). This means that MOF-501 is kinetically more favorable, and MOF-502 is thermodynamically more preferred product [46].

The structure of metallosupramolecular network is greatly affected by the solvent system as mentioned earlier. In particular it happens when the solvent molecules are involved in the network as the guest molecules or coordinating ligands. For example, $[Zn_4O(NTB)_2]_n\cdot3n$DEF·nEtOH (**1**-**2**), which has a doubly interpenetrated (3,6)-connected PdF_2 net structure, was isolated from the solvothermal reaction of $Zn(NO_3)_2\cdot6H_2O$ and 4,4′,4″-nitrilotrisbenzoic acid (H_3NTB) at 110 °C in a mixture of $DEF/EtOH/H_2O$ (5/3/2, v/v) for 24 h [36]. However, in EtOH solvent system, the solvothermal reaction of the same metal and organic building blocks offers the different network. It produces

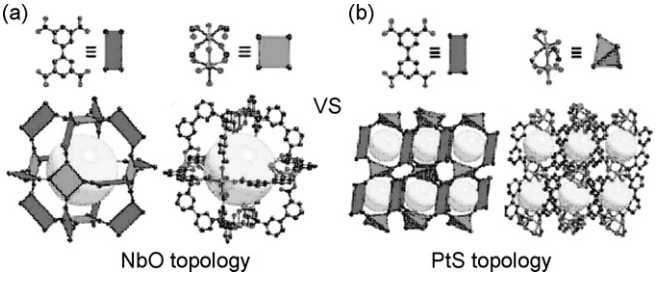

Fig. 10. (a) The crystal structure of $[Co_2(BPTC)(H_2O)_5]\cdot G_x$ (MOF-501, **1**-**9**) showing square BPTC and square $Co_2(CO_2)_4$ building unit to form an NbO net. (b) The crystal structure of $[Co_2(BPTC)(H_2O)(DMF)_2]\cdot G_x$ (MOF-502, **1**-**10**) showing square BPTC and distorted tetrahedral $Co_2(CO_2)_4$ building unit to form a PtS net. Reproduced with permission from Ref. [46].

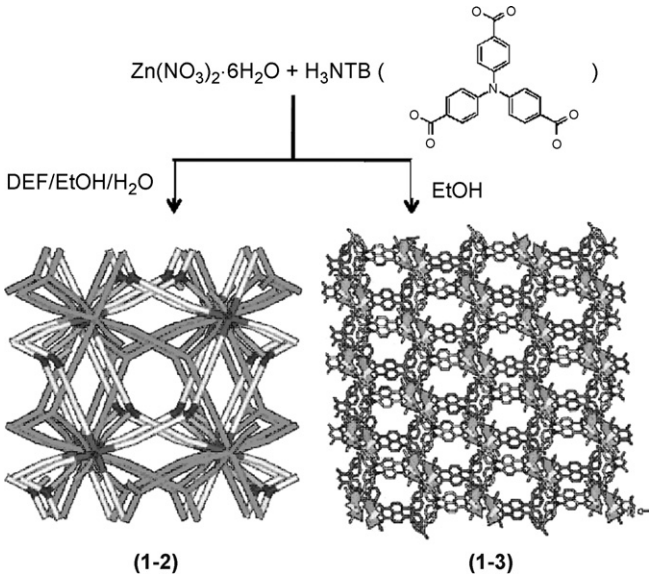

Fig. 11. Two different 3D networks prepared from the solvothermal reactions of Zn(II) and H_3NTB in different solvent systems. Reproduced with permission from Refs. [36,37].

$[Zn_3(NTB)_2(EtOH)_2]_n\cdot4n$EtOH (**1**-**3**), which has 3D network generating 1D channels of honeycomb aperture (Fig. 11) [37]. Due to these complexities, the rational design and synthesis of metallosupramolecular network are sometimes very difficult despite the recent extensive studies.

2.3. Self-assembly of macrocyclic complexes and organic building blocks

In the assembly of metallosupramolecular network, utilization of macrocyclic complex as a metal building block offers several advantages over free metal ions. Free metal ion contains many binding sites for the organic ligands, and thus the extending direction of the network cannot be easily controlled. However, the macrocyclic complexes in square-planar geometry contain only two vacant coordination sites at the *trans* positions, thereby acting as the linear linkers for the organic ligands. Therefore, the utilization of macrocyclic complexes simplifies the design of the network structures. When the organic ligand is assembled with a macrocyclic complex in square planar geometry, organic units locate at the nodes of the network to determine the network structure, contrary to the common coordination networks where metal building units are located at the nodes. Furthermore, macrocyclic complexes are able to prevent the interpenetration of the network that can be a major impediment in the construction of open structures, due to the bulkiness of the ligands [47].

Suh's group initiated and has developed construction of porous metallosupramolecular networks by utilizing macrocyclic complexes and carboxylate ligands [11–16,47–55]. The networks thus prepared are able to exhibit porosity, H_2 gas storage capabilities [48,54], and selective guest binding properties for various guest molecules [11,12,15,16,48,49]. Many of them show single-crystal-to-single-crystal transformations on

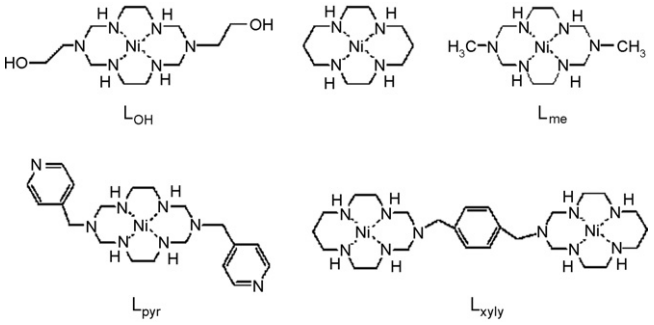

Scheme 2. Various macrocyclic complex.

removal and reintroduction of guest molecules, which involve changes in the network structures by the dynamic motions of the molecular components [11,12,55,56]. In addition, the networks incorporating Ni(II) macrocyclic species can be utilized in the preparation of mono-dispersed and small sized metal nanoparticles based on the redox reactions with metal ions such as Ag(I), Au(III), and Pd(II) [54,55,79].

Various metallosupramolecular networks have been prepared by utilizing macrocyclic complexes as metal building blocks and dicarboxylates [48,52,54], tricarboxylates [11,12,14–16,49–51], and tetracarboxylates [13,55] as organic building blocks. The macrocyclic complexes employed in the assembly of the networks are described in Scheme 2.

When linear dicarboxylate ligands are linked by the Ni(II) macrocyclic complex in a square-planar geometry, 1D chains are formed. In the solid state, the 1D chains can be packed in various modes. In most cases, they pack in a parallel manner to provide nonporous structure. However, when the molecular building blocks have appropriate shapes and lengths, the 1D chains would pack in different way to generate pores or channels. Various rod-packing modes have been mathematically analyzed in the literature [57].

When Ni(II) macrocyclic complex with hydroxyl pendants $[Ni(L_{OH})]^{2+}$ and Na_2BDC (sodium benzenedicarboxylate) were self-assembled in MeCN/H_2O, a 1D coordination polymer chain $\{[Ni(L_{OH})](BDC)\}_n{\cdot}4nH_2O$ (**2-1**, L_{OH} = Ni(II) macrocyclic complex with hydroxyl pendents = $C_{12}H_{30}N_6O_2$) was formed [52] (Fig. 12). In the solid state, two different series of 1D chains extended in different directions and were packed alternately in a manner similar to the plywood generating 1D channels. The 1D chains were interconnected by the hydrogen-bonding interactions between the pendant hydroxyl groups of the macrocycles belonging to a polymer chain and the secondary amines of the macrocycles belonging to the other polymer chain.

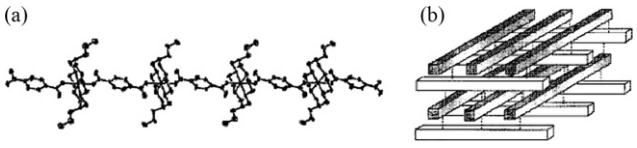

Fig. 12. (a) 1D linear coordination polymer chain constructed of $[Ni(L_{OH})]^{2+}$ and BDC^{2-}. (b) Schematic diagram of **2-1** showing the packing mode of 1D chains to generate channels. Reproduced with permission from Ref. [52].

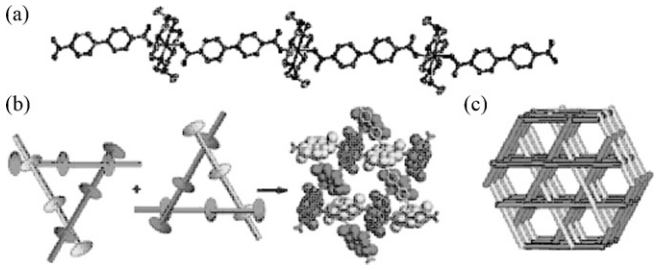

Fig. 13. (a) 1D linear coordination polymer chain. (b) Double network of threefold braids where macrocycles fit into the grooves created by $bpydc^{2-}$ or $bpdc^{2-}$. (c) A view showing the stacking of the linear chains to generate 1D honeycomb channels. Reproduced with permission from Refs. [48,54].

When Ni(II) complexes of macrocyclic ligands L and L_{me} (L = 1,4,8,11-tetraazacyclotetradecane, and L_{me} = 3,10-dimethyl-1,3,5,8,10,12-hexaazacyclotetradecane), respectively, were self-assembled with longer dicarboxylates such as $bpydc^{2-}$ (2,2′-bipyridyl-5,5′-dicarboxylate) and $bpdc^{2-}$ (4,4′-biphenyldicarboxylate), 3D porous networks $\{[Ni(L)](bpydc)\}_n{\cdot}5nH_2O$ (**2-2**) and $\{[Ni(L_{me})](bpdc)\}_n{\cdot}2npyr{\cdot}6nH_2O$ (**2-3**) (pyr = pyridine) resulted due to the packing of the 1D chains [48,54]. Since $bpydc^{2-}$ and $bpdc^{2-}$ ligands are planar and locate almost perpendicularly to the macrocyclic coordination plane, grooves are formed in the 1D chains between the macrocycles. In the crystal structures of **2-2** and **2-3**, three series of 1D chains extend in three different directions, and they pack in the form of a double network of threefold braids [57], where all macrocycles and grooves fit in the key-and-lock style (Fig. 13). The packing generates 1D channels with honeycomb aperture, and these porous structures are extremely robust and the frameworks are retained even after several cycles of dehydration and rehydration processes. They exhibit permanent porosity, H_2 gas storage capability, and selective guest binding properties.

The 2D networks have been constructed by using macrocyclic complexes and organic tricarboxylate ligands [11,12,14–16,49–51]. In honeycomb-like 2D networks, triangular building blocks are placed at every corner of a hexagon and linked by the macrocyclic complexes as the linear linkers. In particular, when Ni(II) or Cu(II) macrocyclic complexes are self-assembled with tricarboxylate ligands in a 3:2 stoichiometry, a neutral network with honeycomb or brickwall cavities is formed, depending on the coordination mode of the tricarboxylate ligands. If the layers are stacked by the interlayer interactions such as hydrogen-bonding or π–π stacking interactions to align the pores, channels are generated.

The pore size of the network depends on the size of the tricarboxylate ligands. Mathematically, the diagonal length of the honeycomb cavity is four times of the length of an arm of the tricarboxylate. That is, if a tricarboxylate ligand with an arm length of *l* Å is used as an organic building block, the resulting structure would contain hexagonal cavities with a diameter of 4*l* Å (Scheme 3).

By the self-assembly of various Ni(II) macrocyclic complexes and benzenetricarboxylate (BTC^{3-}), 2D networks $\{[Ni(L_1)]_3[BTC]_2\}_n{\cdot}18nH_2O$ (**2-4**), $\{[Ni(L_1)]_3[BTC]$

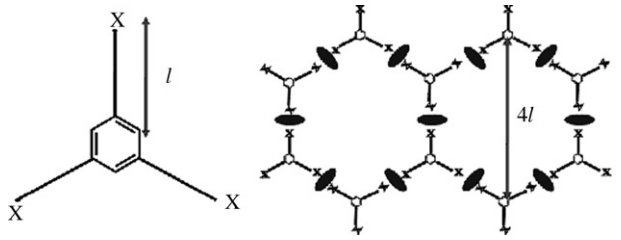

Scheme 3. Relationship between the length of triconnecting ligand and the cavity size of honeycomb layer.

$_2\}_n\cdot 14n H_2O\cdot 2n$pyr (**2-5**), $\{[Ni(L)(H_2O)_2]_3[BTC]_2\}_n\cdot 24nH_2O$ (**2-6**), and $\{[Ni(L_{me})]_3[BTC]_2\}_n\cdot 18nH_2O$ (**2-7**) were constructed. By the self-assembly of Cu(II) macrocyclic complex and benzenetricarboxylate, $\{[Cu(L_{me})]_3[BTC]_2\}_n\cdot 18nH_2O$ (**2-8**) was prepared (Fig. 14) [15,16,49,50]. In these 2D networks, pore shape and size of networks as well as packing modes are greatly affected by the type of macrocycle, metal ion, the size of the tricarboxylate ligand, and the solvent system.

The self-assembly of a square-planar Ni(II) macrocyclic complex containing hydroxyl pendant chains $[Ni(L_{OH})]^{2+}$ and Na_3BTC in H_2O/DMF results in a 2D metallosupramolecular network $\{[Ni(L_{OH})]_3[BTC]_2\}_n\cdot 18nH_2O$ (**2-4**) having brick-wall cavities. However, in presence of pyridine a 2D coordination polymer with honeycomb cavities $\{[Ni(L_{OH})]_3[BTC]_2\}_n\cdot 14nH_2O\cdot 2n$pyr (**2-5**) is formed [50]. The effective cavity sizes of **2-4** and **2-5** with the consideration of van der Waals surfaces are ca. 6.7 Å × 13 Å and 11.4 Å × 11.4 Å, respectively. The formation of different cavity shapes in **2-4** and **2-5** is attributed to the different coordination modes of the BTC^{3-} anion. The BTC^{3-} coordinates metal ions via C_1 symmetry in **2-4**, while it coordinates metal ions via C_3 rotational symmetry in **2-5**. The symmetrical binding mode of BTC^{3-} in **2-5** is induced by the π–π interactions with the pyridine molecules included between the layers. The XRPD patterns for the desolvated solids indicate that the structural changes occur on removal of guest molecules.

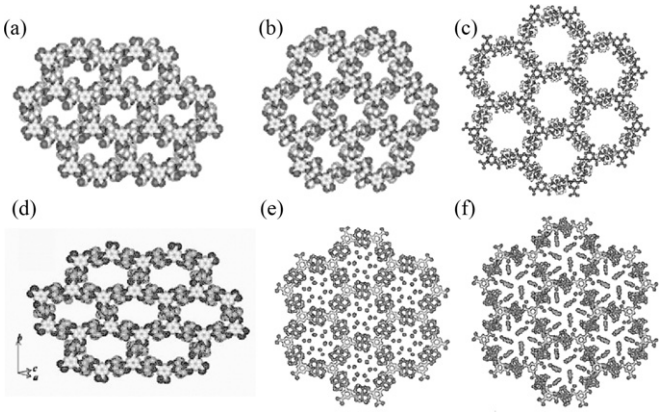

Fig. 14. (a) CPK representation of the 2D layers of **2-4** with the brick-wall cavities. (b) CPK representation of the 2D layers for **2-5** with honeycomb-like cavities. (c) A view of **2-6** seen on the *ab* plane. Water molecules included in the channels are omitted for clarity. (d) CPK representation showing the topview of a 2D layer of **2-7**. (e) X-ray crystal structure of **2-8**. (f) Top view of **2-8′**. Reproduced with permission from Refs. [15,16,49,50].

A 3D network $\{[Ni(L)(H_2O)_2]_3[BTC]_2\}_n\cdot 24nH_2O$ (**2-6**) was assembled from $[Ni(L)]^{2+}$ and BTC^{3-} [15]. In the network, each Ni(II) macrocyclic complex coordinates water molecules, which form hydrogen bonds with two BTC^{3-} units above and below the macrocyclic plane, and each BTC^{3-} interacts with three Ni(II) units. Thus, the positively charged macrocyclic complex layers and negatively charged organic layers are alternately packed closely (3.70 Å), leaving no open spaces on the side directions. The network generates 1D channels of honeycomb aperture whose effective window size is 10.3 Å in diameter. The powder X-ray diffraction (XRPD) pattern of the desolvated solid exhibits a deformed framework structure. However, when the desolvated solid is suspended in water for 5 min, the same XRPD pattern as that of the original crystal (**2-6**) is regenerated. The desolvated solid differentiates glucose versus maltose.

When the Ni(II) and Cu(II) macrocyclic complexes, respectively, were assembled with BTC^{3-}, 2D networks $\{[Ni(L_{me})]_3[BTC]_2\}_n\cdot 18nH_2O$ (**2-7**) and $\{[Cu(L_{me})]_3[BTC]_2\}_n\cdot 18nH_2O$ (**2-8**) resulted [16,49]. These network structures are similar to that of **2-5**. In **2-7**, the carboxylate groups of BTC^{3-} are directly coordinated to $[Ni(L_{me})]^{2+}$ ions, which affords a 2D network with brick-wall cavities. The 2D networks are packed to generate 1D channels of effective aperture size of 12.5 Å × 6.8 Å. A few lines in the XRPD pattern are broadened when crystal is heated at 100 °C for 1 h, but their positions are unaltered. When water vapor is diffused to the desolvated solid, the XRPD pattern same as that of the original crystal is restored. In $\{[Cu(L_{me})]_3[BTC]_2\}_n\cdot 18nH_2O$ (**2-8**), the carboxylate groups of BTC^{3-} are directly coordinated to $[Cu(L_{me})]^{2+}$ units to result in honeycomb like 2D layers, which are packed to generate 1D channels [16]. On dissolution of **2-8** in an aqueous solution of phenol, a hybrid solid $\{[Cu(L_{me})]_3[BTC]_2\}_n\cdot 9n$PhOH$\cdot 6nH_2O$ (**2-8′**) is formed, in which highly ordered 2D noncovalent phenol layers are alternately packed with the host metallosupramolecular layers in the crystal lattice. The phenol layers are formed by the edge-to-face π–π interactions between the phenol molecules.

The self-assembly of tricarboxylate CTC^{3-} (*cis*,*cis*-1,3,5-cyclohexanetricarboxylate) and Ni(II) macrocyclic complex of L_{pyr} (L_{pyr} = hexaazamacrocyclic complex having pyridyl pendents) in water in the presence of triethylamine, provides network solid $\{[Ni(L_{pyr})]_3[CTC]_2\}_n\cdot 16nH_2O$ (**2-9**) (Fig. 15) [14]. Solid **2-9** consists of puckered honeycomb-like layers.

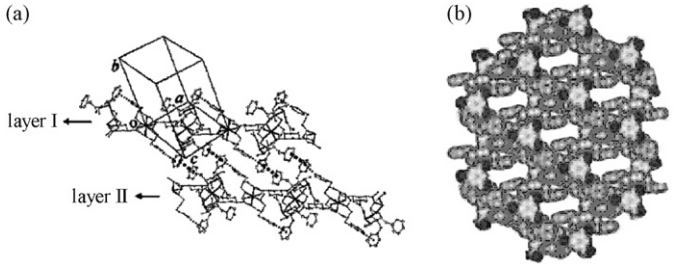

Fig. 15. (a) Side view of 2D layers of **2-9**. The π–π stacking interactions are indicated by lines for intralayer interactions and by ··· lines for interlayer interactions. (b) CPK representation of a single layer of **2-9**. The effective void size is ca. 4.0 Å × 8.5 Å. Reproduced with permission from Ref. [14].

Between the layers, the pendant pyridine rings of the macrocycles are involved in the offset π–π stacking interactions to result in a 3D structure. The XRPD pattern indicates that the structure of **2-9** is deformed when the guest water molecules are removed, but the original structure is restored upon rebinding of water.

Although macrocyclic complexes generally provide non-interpenetrating networks, they form interpenetrated or interwoven structures with considerably large tricarboxylate ligands [13,51]. For example, when a long tricarboxylate organic building block, $TCPEB^{3-}$ (1,3,5-tris[2-(4-carboxylphenyl)-1-ethynyl]benzene) is employed in the self-assembly with Ni(II) macrocyclic complex in the mixture of DMF/H_2O/pyridine (1.5/2/3, v/v), $\{[Ni(L)]_3[TCPEB]_2\}_n \cdot 6npyr\cdot 4nH_2O$ (**2-10**) is formed, in which 2D honeycomb-like layers with big cavities (ca. 49–53 Å) are triply interwoven to form a borromean layer generating smaller triangular voids (ca. 18.4 Å × 14.7 Å × 9.5 Å) (Fig. 16) [51].

When Ni(II) bismacrocyclic complex $[Ni_2(L_{xyly})]^{4+}$ and BTC^{3-} were self-assembled, a bilayer network $\{[Ni_2(L_{xyly})]_3[BTC]_4\}_n \cdot 6npyr\cdot 36nH_2O$ (BOF-1, **2-11**; $L_5 = C_{26}H_{52}N_{10}$) was assembled [11]. In **2-11**, the 2D layers have brick-wall cavities of size 23 Å × 14 Å and the xylyl groups of the bismacrocyclic complexes act as the pillars linking the two layers to form pillared bilayer network generating 3D channels. The interlayer distance of the bilayer is ca. 11.9 Å and the side window is 14.5 Å. The structure has void volume of 61% as estimated by PLATON (Fig. 17). Interestingly, when the single crystal of **2-11** was dried in air and then heated at 75 °C for 1.5 h, respectively, the single-crystal to single-crystal transformations occurred to provide $\{[Ni_2(L_{xyly})]_3[BTC]_4\}_n \cdot 30nH_2O$ (**2-11′**) and $\{[Ni_2(L_{xyly})]_3[BTC]_4\}_n \cdot 4nH_2O$ (**2-11″**). The X-ray crystal structures revealed a sponge-like behavior of the bilayer network that reduced the interlayer distance in response to the amount of guest molecules.

When tetrahedral organic building blocks are connected by the Ni(II) macrocyclic complexes, a diamondoid network with adamantanoid cages is formed. For example, the self-assembly of $[Ni(L)](ClO_4)_2$ and Na_4TCM (TCM = tetrakis[4-(carboxyphenyl)-oxamethyl]methane) in DMF/H_2O (1:1, v/v) results in $\{[Ni(L)]_2[TCM]\}_n \cdot 2nDMF\cdot 10nH_2O$ (**2-12**) (Fig. 18) [13]. In **2-12**, each Ni(II) ion is coordinated with two different TCM^{4-} at the axial sites to exhibit a distorted octahedral coordination geometry, and each TCM^{4-} ligand binds four $[Ni(L_2)]^{2+}$ complexes in a tetrahedral manner, which gives rise to a diamondoid network comprising large adamantanoid cages of

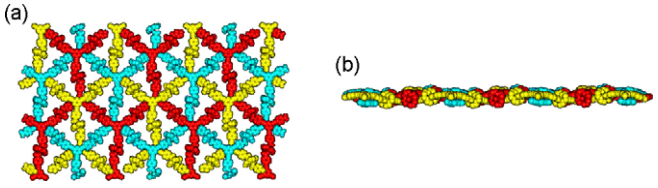

Fig. 16. X-ray structure of $\{[Ni(L)]_3[TCPEB]_2\}_n \cdot 6npyr\cdot 4nH_2O$ (**2-10**). (a) Top view and (b) side view, showing threefold interwoven (6,3) nets. Reproduced with permission from Ref. [51].

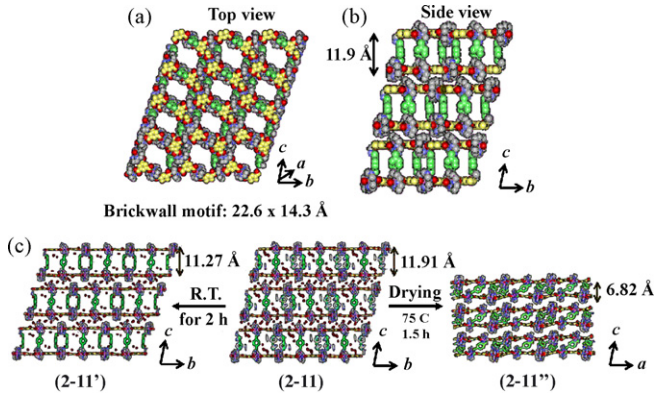

Fig. 17. (a) X-ray structure of **2-11**, showing 2D layers of a brick-wall motif. (b) Side view showing the pillared-bilayer structure (bilayer distance, 11.91(1) Å). (c) Single crystal to single crystal transformation of **2-11**, exhibiting sponge-like behavior. Color scheme: Ni, pink; O, red; N, blue; C of macrocycle, gray; C of BTC^{3-}, yellow; C of pillars, green. Guest water and pyridine molecules are omitted for clarity. Reproduced with permission from Refs. [11,12].

size 49.2 Å × 50.8 Å × 44.3 Å (the longest intracage distances). Such a large cavity induces an unusual eightfold interpenetration of the networks in the [4 + 4] mode. Despite the high-fold interpenetration, the network generates 1D channels with an effective window size of 6.7 Å × 4.7 Å. The network exhibits a flexible behavior: it becomes nonporous on removal of the guest molecules that occupy the channels, as verified by the N_2 gas sorption measurement. However, the open structure is restored when the desolvated solid is immersed in a mixture of H_2O/DMF (1:1, v/v) for 5 min, as evidenced by the XRPD patterns.

The self-assembly of tetracarboxylate $BPTC^{4-}$ (1,1′-biphenyl-2,2′,6,6′-tetracarboxylate) with Ni(II) macrocyclic complex provides a square grid network $\{[Ni(L)]_2[BPTC]\}_n \cdot 2$

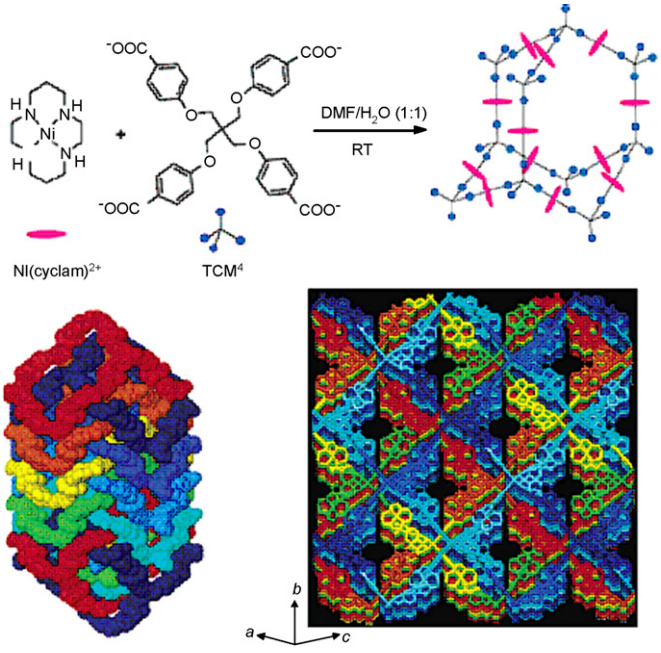

Fig. 18. The X-ray structure of eightfold interpenetrating diamondoid network, $\{[Ni(L)]_2[TCM]\}_n \cdot 2nDMF\cdot 10nH_2O$ (**2-12**). Reproduced with permission from Ref. [13].

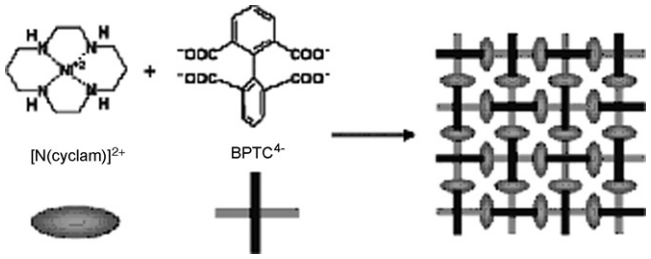

Scheme 4. Construction of square grid network.

nH$_2$O (**2-13**) (Scheme 4). In the crystal structure (Fig. 19), the two phenyl rings of a BPTC^{4-} unit are twisted almost perpendicularly with respect to each other (dihedral angle, 77.9(2)°), and thus each BPTC^{4-} acts as the planar four-connecting organic building block to coordinate four Ni(II) macrocyclic complexes. The size of the square compartment in the square grid network is 10 Å × 11 Å and the effective void size is 1 Å × 1 Å. The water guest molecules are intercalated between the layers instead of inside the square compartments. The void volume is about 12% of the total crystal volume, as estimated by PLATON [55].

3. Gas storage and separation

One of the important functions of metallosupramolecular networks is adsorption of gases. If the networks adsorb any gas, they are regarded as porous materials. However, metallosupramolecular networks often collapse when the guest molecules occupying the voids are removed [14,15,51]. Only the robust porous networks that are stable even after guest removal adsorb gases. In some cases, even though the networks collapse on guest removal, the solids adsorb gas molecules at high pressures and restore the original porous structures [58]. There are flexible metallosupramolecular networks that adsorb gases by changing the pore sizes and channels [59,60].

Permanent porosity of a metallosupramolecular network should be demonstrated by the measurement of gas sorption isotherms, typically using N_2 gas at its normal boiling point. All porous metallosupramolecular networks reported to date are microporous by IUPAC definition [61], having cavities less than 2 nm in size and displaying type I isotherms. The surface area and pore volume of the networks can be estimated from the gas sorption data.

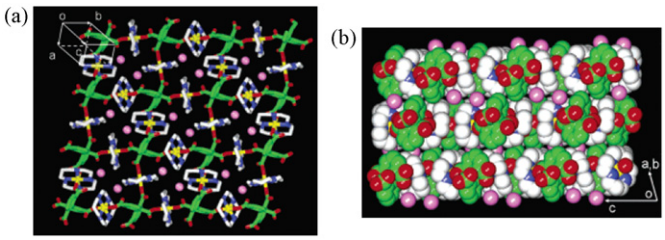

Fig. 19. X-ray crystal structure of $\{[Ni(L)]_2[BPTC]\}_n \cdot 2nH_2O$ (**2-13**). (a) Top view seen on the (1 1 0) plane, showing the 2D square grid network. (b) Side view (in CPK) showing the stacking of the 2D layers. Color scheme: Ni, yellow; O (BPTC), red; N, blue; C (cyclam), white; C (BPTC), green; guest water, pink. Reproduced with permission from Ref. [55].

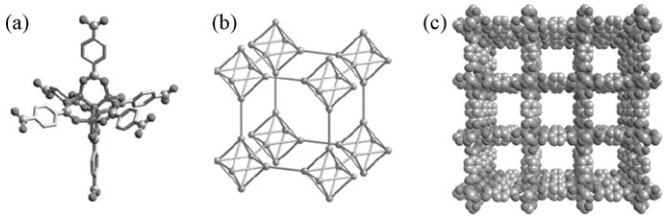

Fig. 20. (a) Octahedral secondary building unit of $Zn_4O(CO_2)_6$ in the crystals of IRMOF-1. (b) A primitive cubic lattice. (c) Porous structure generating cubic channels. Reproduced with permission from Ref. [63].

Type I gas isotherm is often described by the Langmuir model, which assumes that a homogenous monolayer of the adsorbate is formed on the walls of the porous solid. An extension to this model to multilayer adsorption is the commonly used Brunauer–Emmett–Teller (BET) equation, which is primarily used to determine the point at which monolayer coverage is obtained. In either case, the apparent surface area can be calculated. The micropore volume, usually calculated by the Dubinin–Radushkevich (DR) method, is a complementary and perhaps better description of the porosity of a material [62].

3.1. Gas sorption in rigid porous networks

Metallosupramolecular networks often collapse when the guest molecules occupying the voids are removed, which offers a serious problem in application. Yaghi et al. reported many robust networks, which showed permanent porosity with large pore volume and large surface area [31]. Representative examples are a series of cubic porous networks that are constructed from the octahedral $Zn_4O(CO_2)_6$ secondary building unit and linear dicarboxylate linkers (Fig. 20) [32]. The IRMOF series show high surface area and large pore volume (Table 1).

Férey et al. reported many porous network solids that had very large pore size and surface area. The network structures were determined mainly by Rietveld refinements by using powder X-ray diffraction data, and the guest species were refined by Fourier difference maps [64,65]. A representative example is $Cr_3F(H_2O)_2O[(O_2C)\text{-}C_6H_4\text{-}(CO_2)]_3 \cdot nH_2O$ (where n is 25, MIL-101, **3-1**), which can be prepared from 1,4-BDC anions and inorganic trimers containing three chromium atoms (Fig. 21) [64]. It showed permanent porosity with large pore volume (2.01 cm^3/g) and large surface area (4100 m^2/g by BET equation, 5900 m^2/g by Langmuir equation).

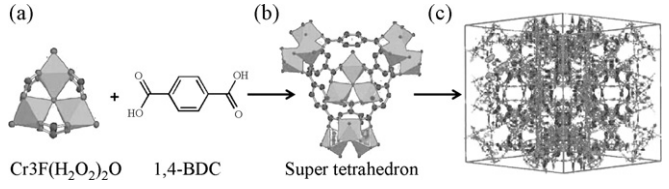

Fig. 21. (a) The computationally designed chromium trimeric building block and 1,4,-BDC organic building block. (b) A super tetrahedron (ST) consisting of trimeric chromium and BDC^{2-}. (c) A ball and stick representation of one unit cell. Reproduced with permission from Ref. [64].

Table 1
Porosity of various metallosupramolecular networks estimated by N_2 gas sorption data at 77 K

Compound	Formula	Surface area (m^2/g)[a]	Pore volume (cm^3/g)[b]	Reference
IRMOF-1	$[Zn_4O(BDC)_3]$	3362	1.19	[63]
IRMOF-6	$[Zn_4O(R^6\text{-}BDC)_3]$	2630	0.93	[32]
IRMOF-8	$[Zn_4O(NDC)_3]$	1466	0.52	[32]
IRMOF-11	$[Zn_4O(HPDC)_3]$	1911	0.68	[32]
IRMOF-14	$[Zn_4O(PDC)_3]$	4923	0.42	[32]
IRMOF-18	$[Zn_4O(TMBDC)_3]$	1501	0.53	[67]
IRMOF-20	$[Zn_4O(TTDC)_3]$	4346	1.53	[68]
MOF-74	$Zn_3[O_3(DHBDC)_3]$	1070	0.39	[69]
MOF-505	$[Cu_2(BPTC)]$	1830	0.63	[57]
MOF-177	$[Zn_4O(BTB)_2]$	4500	1.59	[70]
1-**1**′	[Mn(NDC)]	191	0.068	[33]
1-**2**′	$[Zn_4O(NTB)_2]$	1121	0.51	[36]
1-**3**′	$[Zn_3(NTB)_2]$	419	0.14	[37]
2-**2**′	$\{[Ni(L)](bpydc)\}_n$	817	0.37 cm^3/cm^3	[48]
2-**3**′	$\{[Ni(L_{me})](bpdc)\}_n$	691	0.39	[54]
3-**1** (MIL-101)	$Cr_3F(H_2O)_2O[BDC]_3$	5900	2.01	[64]
3-**2** (MIL-100)	$Cr_3F(H_2O)_2O[BTC]_3$	3100	1.16	[65]
3-**3**	$[Cu_2L^1]$	1670[c]	0.68	[66]
3-**4**	$[Cu_2L^2]$	2247[c]	0.89	[66]
3-**5**	$[Cu_2L^3]$	2932[c]	1.14	[66]

[a] Surface area estimated by Langmuir equation.
[b] Pore volume estimated by DR (Dubinin–Radushkevich) method.
[c] Estimated by BET equation.

They also reported MIL-100 (**3**-**2**), which had a similar structure to MIL-101 (**3**-**1**) except that BTC^{3-} (1,3,5-benzenetricarboxylate) was contained instead of BDC^{2-} (1,4,-benzenedicarboxylate) as an organic linker. The N_2 isotherm of **3**-**2** is between type I and type IV with a slightly secondary uptake, which is indicative of the presence of both micro- and meso-pores. The pore volume is 1.16 cm^3/g and Langmuir surface area is 3100 m^2/g [65].

Schröder and co-workers reported porous networks consisting of tetracarboxylate organic linkers and $[Cu_2(RCOO)_4]$ paddle-wheel secondary building units [66]. In the structures, each $[Cu_2(RCOO)_4]$ paddle-wheel is linked to four biphenyl (H_4L^1, **3**-**3**), terphenyl (H_4L^2, **3**-**4**), or quaterphenyl (H_4L^3, **3**-**5**) connectors to provide the networks with NbO-type topologies, which generate pores of size 6.5, 7.3, and 8.3 Å, respectively. The gas sorption data for a series of networks indicate that longer organic building blocks generate better porosity (Fig. 22 and Table 1).

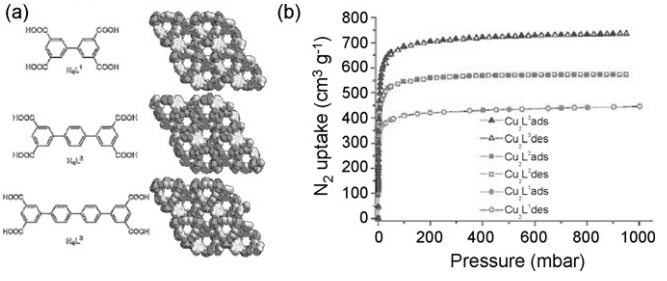

Fig. 22. (a) Organic building blocks and network structures of **3**-**3**, **3**-**4**, and **3**-**5**. (b) N_2 sorption isotherms measured for desolvated compounds at 78 K. ads = adsorption, des = desorption. Reproduced with permission from Ref. [66].

Suh and co-workers reported porous networks such as **1**-**1**, **1**-**2**, **1**-**3**, **2**-**2**, **2**-**3**, as described in the earlier part of this paper. They showed remarkable gas sorption properties. These gas sorption data are summarized in Fig. 23 and Table 1 [33,36,37,48,54].

3.2. Gas sorption in flexible networks

Kitagawa et al. reported the flexible and dynamic networks that collapsed on removal of guest solvent molecules but restored the porous structures by adsorption of gas molecules at high pressures. The typical gas sorption isotherm for dynamic porous materials is presented in Fig. 24. At low pressure, the type II

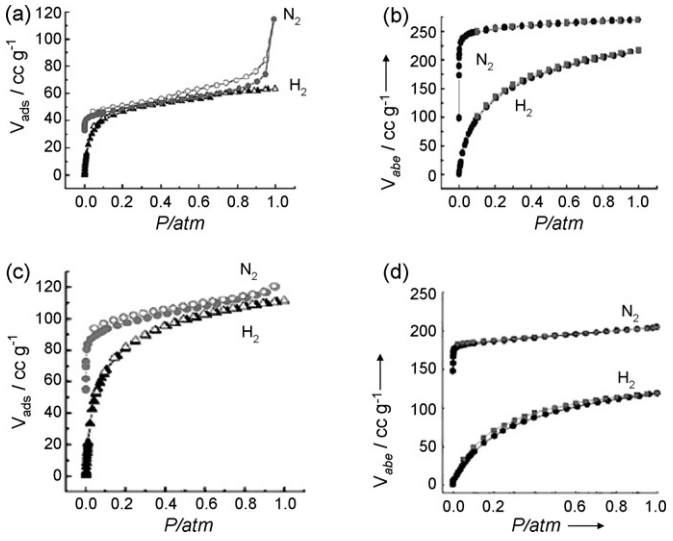

Fig. 23. N_2 and H_2 sorption isotherms measured at 77 K for (a) **1**-**1**′, (b) **1**-**2**′, (c) **1**-**3**′, and (d) **2**-**2**′. Reproduced with permission from Refs. [33,36,37,48].

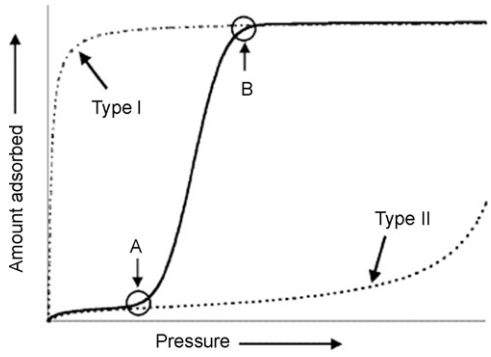

Fig. 24. Adsorption isotherms observed when porous networks undergo a transformation from nonporous to porous structure. Dashed lines represent the type I and type II isotherms. Points A and B indicate the gate-opening and gate-closing pressures which accompany the start and end of the structure transformation, respectively. Reproduced with permission from Ref. [59].

gas isotherm is exhibited, indicating a nonporous phase. After a certain point A, the isotherm begins to approach type I with a steep rise, indicating a porous phase. The structural transformation from nonporous to porous phase proceeds till the isotherm reaches to point B. This sharp adsorption jump/desorption drop with the hysteresis indicates the occurrence of a network transformation in the solid state. The point of jump is referred as gate-opening pressure, at which guest accommodation starts [59,60].

They reported $[Cu(dhbc)_2(4,4'\text{-bpy})]_n{\cdot}_nH_2O$ (CPL-p1, **3-6**) (dhbc = 2,5-dihydroxybenzoic acid, 4,4′-bpy = 4,4′-bipyridine) and $[Cu(BDC)(4,4'\text{-bpy})_{0.5}]_n$ (CPL-v1, **3-7**), which are the interdigitated 2D network and the interpenetrated 3D network, respectively [58]. The compounds underwent drastic structural transformations upon guest removal and uptake, which were monitored by the measurement of XRPD patterns and gas sorption isotherms (Fig. 25). The XRPD patterns showed that on dehydration the length of *c*-axis of CPL-p1 (**3-6**) was contracted from 15.863(2) Å to 11.171(14) Å, which corresponded to a cell-volume contraction of 27%. It was suggested that the shrinkage of the layer gap occurred through a glide motion of the two π-stack ring moieties of dhbc ligand and concomitant decrease in the channel cross section. The re-expansion of the shrunk structure occurred on exposure to N_2 gas below 160 K. Gas sorption isotherms for CO_2, CH_4, O_2 and N_2 measured for **3-6** at high pressures and ambient temperature showed characteristic hysteretic loops (Fig. 25), which must be attributed to expansion and contraction of the crystal structure triggered by gas adsorption and desorption, as confirmed by XPRD. The differences in the gate-opening and the gate-closing pressures for CO_2, O_2, and N_2 gases were explained by the differences in the intermolecular interaction force of the guest molecules. Similar adsorption behavior was observed also for CPL-v1 (**3-7**).

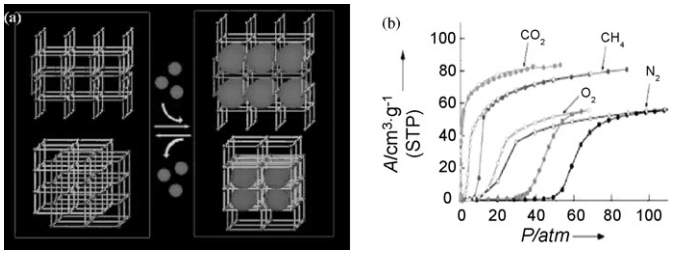

Fig. 25. (a) Schematic representation of dynamic structural changes of the networks depending on the guest molecules. (b) Adsorption (filled circles) and desorption (open circles) isotherms of N_2, CH_4, CO_2 and O_2 for desolvated solid $[Cu(dhbc)_2(4,4'\text{-bpy})]_n$ (**3-6′**) at 298 K. Reproduced with permission from Ref. [58].

Solvothermal reaction of $Co(SCN)_2$ and organic building block, 4-peia (4-peia = *N*-(2-pyridine-4-yl-ethyl)-isonicotinamide), affords 3D network $\{[Co(NCS)_2(4\text{-peia})_2]{\cdot}4Me_2CO\}_n$ (**3-8**) by the complementary hydrogen bonds between the 2D layers [71]. X-ray powder diffraction patterns indicate that the network shows amorphous (nonporous)-to-crystal (porous) structural rearrangement on desorption and adsorption processes of Me_2CO, with the retention of the 2D motifs (Fig. 26(a)). The acetone vapor adsorption isotherm, which was measured on desolvated solid over the relative pressure ranged from 0 to 0.9 at 298 K, shows a slight increase and an abrupt rise at $P/P_0 = 0.76$. This characteristic adsorption profile indicates a conversion of the amorphous state to the crystalline state. The desorption isotherm shows a monotonic decrease indicating that the pores are maintained until a sudden drop at $P/P_0 = 0.05$. The large hysteresis implies structural conversion, which is associated with the change of the hydrogen-bonding mode (Fig. 26(b)) [71].

A 2D bilayer $\{[Cu(pyrdc)(bpp)](5H_2O)\}_n$ (**3-9**, pyrdc = pyridine-2,3-dicarboxylate; bpp = 1,3,-bis(4-pyridyl)-propane) shows a reversible sponge-like dynamic behavior upon dehydration and rehydration processes [72]. The XRPD pattern of dehydrated solid shows that positions of some peaks change and some new peaks appear, indicating that structural transformation occurs upon dehydration. Upon exposure of

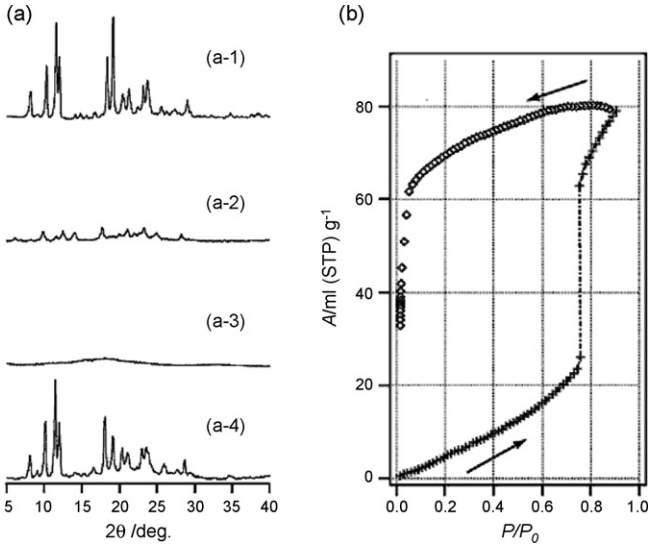

Fig. 26. (a) XRPD patterns of (a-1) as-synthesized, (a-2) desolvated solid by drying in vacuo for 20 h at room temperature, (a-3) desolvated solid by drying in vacuo for 20 h at 373 K, and (a-4) resolvated solid by exposing to an acetone vapor for 4 days. (b) Isotherm for acetone vapor adsorption and desorption at 298 K of **3-8** over the pressure range from 0.507 to 27.756 kPa. P_0 is a saturated vapor pressure, 30.593 kPa, of acetone at 298 K. Reproduced with permission from Ref. [71].

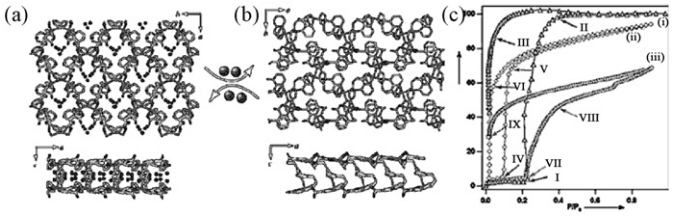

Fig. 27. (a) Honeycomb-like 2D layers of $\{[Cu(pyrdc)(bpp)](5H_2O)\}_n$ (**3-9**) showing a water-filled channel along the *c*-axis (up) and *b*-axis (down). (b) Honeycomb-like 2D layers of dehydrated network along the *c*-axis (up) and *b*-axis (down). (c) Sorption isotherms of $[Cu(pyrdc)(bpp)]_n$ (**3-9′**) for (i) CO_2 (195 K), (ii) MeOH, and (iii) EtOH (298 K) (where P/P_0 is the relative vapor pressure). Reproduced with permission from Ref. [72].

dehydrated solid to water vapor, the original framework is regenerated. The reversible structural transformations are proved also by the single crystal X-ray analyses, which indicate the changes in cell volume, space group, and thickness of the bilayer (Fig. 27). The gas sorption isotherms for O_2 and N_2 at 77 K reveal no inclusion of these gases. However, the solid adsorbs CO_2 gas, regardless of the comparable size to those of O_2 and N_2. The CO_2 gas isotherm shows a sudden increase at point I (relative pressure $P/P_0 = 0.23$) and attains a saturated level at point II ($P/P_0 = 0.41$), at which the gates open. The desorption isotherm does not retrace the adsorption isotherm and shows an abrupt drop at point III ($P/P_0 = 0.04$), which indicates a strong interaction of CO_2 with the host. Similar sorption phenomena were observed for the MeOH and EtOH vapor sorptions (Fig. 27(c)).

3.3. Gas and vapor separation

Separation of small gases and hydrocarbon molecules is important in fuel cell technologies and chemical industries. Microporous metallosupramolecular networks can be applied in separation of small gases such as Ar, N_2, H_2, O_2, CO_2, and CH_4 [34,73,74]. In general, porous solids adsorb gases whose kinetic diameters are smaller than the aperture sizes of the host solids, although other factors such as interactions between the host solid and gas molecules also affect the gas sorption capability. The kinetic diameters of gases are listed in Table 2. Recently separation of hydrocarbons and small organic molecules by utilizing metallosupramolecular networks has been reported [75–77].

Suh and co-workers reported porous metallosupramolecular networks, **1-1′** and **1-3′** and $\{[Ni(L)]_2[MTB]\}_n{\cdot}3n$EtOH (**3-10**) (L = 1,4,8,11-tetraazacyclotetradecane, MTB = methanetetrabenzoate), which exhibited selective gas adsorption properties [33,37,79]. For **1-1′**, adsorption capacities of N_2 and CO_2 gases are higher than that of H_2 in the low-pressure range, indicating that **1-1′** can be applied in the purification of H_2 gas. The removal of small amounts of contaminant gases from H_2 is important for the real use of H_2 gas as a fuel. In addition, adsorption capacity for CO_2 is significantly higher than that of CH_4, which can also be applied in CO_2 removal from the natural gas (Fig. 28) [33].

For **1-3′**, adsorption capability of CO_2 gas is much better than H_2 and CH_4 gases. Therefore, **1-3′** can be applied in H_2 purification as well as CO_2 removal from the natural gas at 195 K (Fig. 29) [37].

Table 2
Dimensional parameters (Å) for various gas molecules [78]

	Length (Å)	Width (Å)	Kinetic diameter (Å)
He		~3	2.6
H_2	3.1	2.4	2.89
Ar		3.84	3.40
O_2	3.9	2.8	3.46
N_2	4.1	3.0	3.64
Kr		3.96	3.60
CO	4.2	3.7	3.76
CO_2	5.1	3.7	3.3
H_2O	3.9	3.15	2.65
NH_3	4.1	3.8	2.6
SO_2	5.28	4.0	3.6
CH_4		4.2	3.8
C_2H_2	5.7	3.7	3.3
C_2H_4	5.0	4.4	3.9

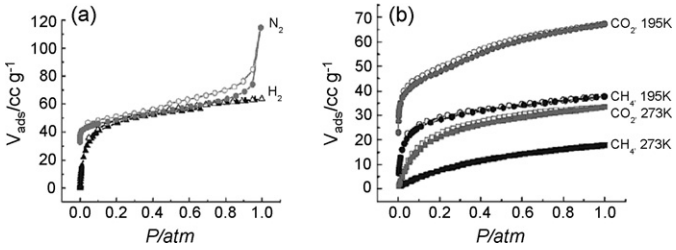

Fig. 28. Gas sorption isotherms of **1-1′**. (a) N_2 and H_2 gas sorption at 77 K. (b) CO_2 and CH_4 sorption at 195 K and 273 K. P_0 (N_2) = 760 Torr. Filled shapes: adsorption. Open shapes: desorption. Reproduced with permission from Ref. [33].

The solid **3-10**, which is a fourfold interpenetrating diamondoid network generating 1D channels, adsorbs H_2, CO_2, and O_2 gases but it does not adsorb N_2 and CH_4 gases. This selective gas sorption property is attributed to the differences in kinetic diameter of the gases. The material can be applied in separation of N_2 and O_2 from air as well as separation of CO_2 and CH_4, and the H_2 enrichment of the N_2/H_2 exhaust mixture resulting from ammonia synthesis (Fig. 30) [79].

Wang and co-workers reported a porous 3D lanthanide-organic framework, $[Er_2(PDA)_3(H_2O)]{\cdot}2H_2O$ (**3-11**) (PDA =

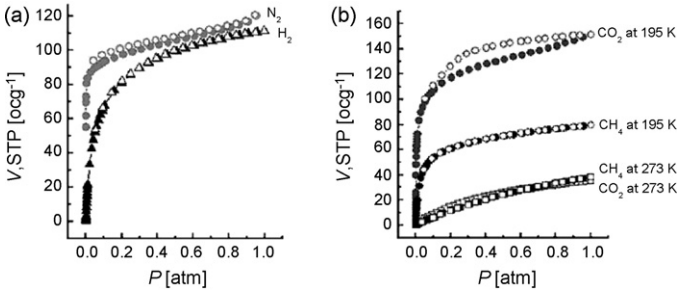

Fig. 29. Gas sorption isotherms of **1-3′**. (a) N_2 and H_2 gas sorption at 77 K. (b) CO_2 and CH_4 gas sorptions at 195 K and 273 K. $P_0(N_2) = 760$ Torr. Filled shapes: adsorption. Open shapes: desorption. Reproduced with permission from Ref. [37].

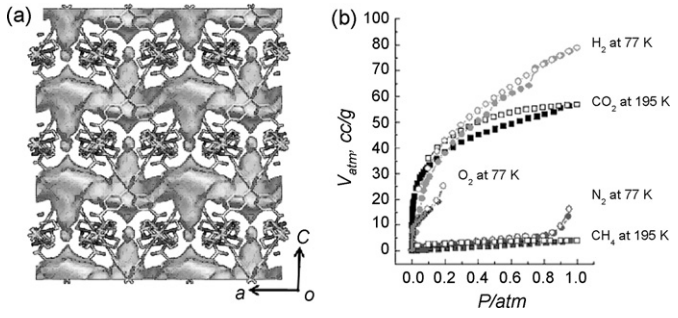

Fig. 30. (a) Surface view seen from the *ac* plane of **3**-**10**. (b) Gas sorption isotherms for **3**-**10**. $P_0(N_2) = 760$ Torr. Fillled shapes, adsorption; open shapes, desorption. Reproduced with permission from Ref. [79].

1,4-phenylenediacetate dianion). When the solid was activated at 200 °C under vacuum, 1D channels with effective window size of ca. 3.4 Å are generated. The desolvated solid exhibited selective adsorption property on CO_2 over Ar and N_2 gases. The selective gas sorption is related with the aperture size of the host and the kinetic diameters of the adsorbate gases. [73].

Zhou and co-workers reported temperature-induced molecular-gating effects in which the size of the gates could be tuned continuously from 2.9 to 5.0 Å [74]. In the network $[Ni_8(5\text{-bbdc})_6(\mu_3\text{-OH})_4]$ (**3**-**12**) (bbdc = *tert*-butyl-1,3,-benzenedicarboxylate), bbdc ligand and octanickel clusters form a trilayer, in which a hydrophilic cluster layer is sandwiched by two hydrophobic bbdc layers. The trilayer, with their exposed hydrophobic exteriors, packs through van der Waals forces, thus generating hydrophobic chambers between adjacent trilayers (Fig. 31(a)). The network generates 1D channels along the *a*-axis, where guest water molecules reside. The network is flexible, and can separate commercially relevant gases such as H_2/N_2, H_2/CO, N_2/O_2, N_2/CH_4, CH_4/C_2H_4, and C_2H_4/C_3H_6. The gas separation capability of the network comes from the bbdc gate in the hydrophilic/hydrophobic interface, which should open wider at higher temperatures due to the thermal vibration of bbdc groups. As the amplitude

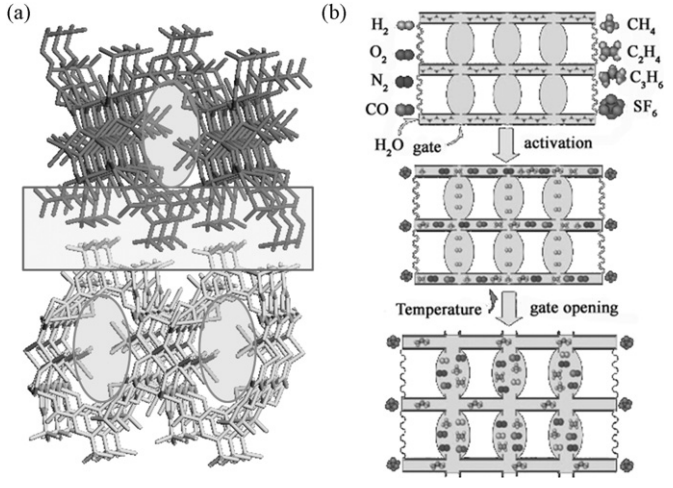

Fig. 31. (a) Two trilayer packed along the *c*-axis to form hydrophobic chambers (square) and hydrophilic channels (circle). (b) Schematic representation of the mechanism of the gating effect. Reproduced with permission from Ref. [74].

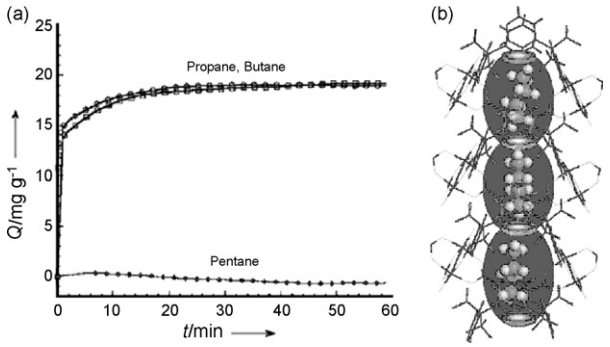

Fig. 32. (a) Adsorption of propane (◯), butane (□), and pentane (◊) at 90 °C and 650 Torr in **3**-**13** as a function of time. *Q* is the weight of hydrocarbon molecules adsorbed in the adsorbent. (b) Arrangement of *n*-butane molecules in the microchannel with one molecule per cage. Reproduced with permission from Ref. [75].

of vibration becomes larger, the wider the gate would open (Fig. 31(b)).

Li and co-workers reported a microporous material, $[Cu(hfipbb)(H_2hfipbb)_{0.5}]$ (**3**-**13**) (H_2hfipbb = 4,4′-(hexafluoroisopropylidene)-bis(benzoic acid)), which is able to separate hydrocarbons [75]. The solid **3**-**13** consists of $[Cu_2(COO)_4]$ paddle-wheel in the equatorial plane and H_2hfipbb ligand in the axial sites to afford 3D network, which has oval-shaped large chambers (the length of the large chamber = 7.3 Å) and narrow windows (the diameter of the neck = 3.2 Å). The network exhibits unique adsorption properties: it can adsorb normal C_2, C_3, and *n*-C_4 olefins and alkanes selectively from all branched alkanes and all normal hydrocarbons above C_4. The narrow neck and length of large chambers are attributed to separate normal hydrocarbon from branched hydrocarbon to show cut-off adsorption for carbon-number (Fig. 32).

Yaghi and co-workers reported doubly interpenetrated framework, MOF-508a, $[Zn(BDC)(4,4\text{-bipy})_{0.5}](DMF)(H_2O)_{0.5}$ (**3**-**14**) (BDC = 1,4-benzenedicarboxylic acid, bipy = 4,4′-bipyridine) having 1D channels (channel size, 4.0 Å × 4.0 Å) [76]. It shows selective adsorption of linear and branched isomers of pentane and hexane when single crystals of desolvated solid $[Zn(BDC)(4,4\text{-bipy})_{0.5}]$ (**3**-**14′**) was used as the GC column material. The column can separate *n*-pentane from *n*-hexane, branched 2-methylbutane from *n*-pentane, and 2-methylpentane, 2,2-dimethylbutane from *n*-hexane, respectively. In addition, the mixture of 2-methylbutane, *n*-pentane, 2,2-dimethylbutane, 2-methylpentane, and *n*-hexane can be easily separated by the column in GC system with different retention time (Fig. 33). The selective GC separation of alkanes is attributed to their different van der Waals interactions with the host due to matching of the size and shape of the alkane with the aperture of the host.

De Vos and co-workers reported separation of mixed C_8 alkylaromatic compounds (*p*-xylene, *m*-xylene, *o*-xylene, ethyl-benzene) by applying $V^{III}(OH)\{O_2C\text{–}C_6H_4\text{–}CO_2\}_2\cdot x(HO_2C\text{–}C_6H_4\text{–}CO_2H)$ ($x = 0.75$) (**3**-**15**), in a GC system [77]. Separation of these compounds is important in the chemical industry, because it is difficult by distillation due to similar

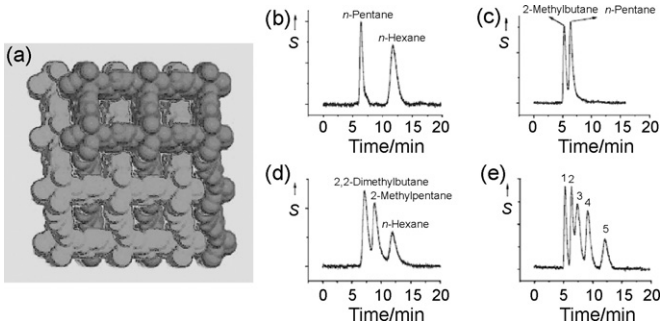

Fig. 33. (a) Space-filling representation of the structure for [Zn(BDC)(4,4-bipy)$_{0.5}$] (**3**-**14**′). Chromatograms of alkane mixtures separated on a column made of **3**-**14**′. (b) Separation of *n*-pentane and *n*-hexane, (c) 2-methylbutane and *n*-pentane, (d) 2,2-dimethylbutane, 2-methylpentane, and *n*-hexane, and (e) separation of an alkane mixture containing 2-methylbutane (1), *n*-pentane (2), 2,2-dimethylbutane (3), 2-methylpentane (4), and *n*-hexane (5). Reproduced with permission from Ref. [76].

boiling point of the compounds (boiling points of *p*-xylene, *m*-xylene, *o*-xylene, and ethyl-benzene are 137–138 °C, 139.3 °C, 144 °C, and 136 °C, respectively). The GC column packed with **3**-**15** can separate mixture of ethylbenzene, *m*-xylene, and *p*-xylene due to the different interaction between the aromatic rings of xylene molecules and the terephthalate ligands and orientation of aromatic rings in the pores of the host [80].

3.4. Hydrogen storage

Hydrogen gas is an excellent energy source and it is non-polluting to form water as a harmless byproduct during use. However, utilization of hydrogen gas as a fuel is difficult due to lack of efficient and safe storage systems. A gram of hydrogen gas occupies about 11 L of space at atmospheric pressure. Thus, the gas must be intensely pressurized to several hundred atmospheres and stored in a pressure vessel. In liquid form, hydrogen can only be stored under cryogenic temperatures. These options are not practical for everyday use [81]. To solve these difficulties, a lot of efforts have been made for the development of hydrogen storage methods [82]. Current storage methods include compression of the gas, cryogenic liquefaction and solidification, adsorption on activated carbon, alloying or compounding with other elements, or combinations of these processes. One of the attractive methods is to find new materials that can store large amounts of H_2 at ambient temperature and relatively low pressures. Metal hydride systems have been intensively examined in this field [81]. The porous solids such as zeolites and activated carbons also displayed appreciable hydrogen gas sorption capacities at 77 K and 1 bar [83].

Since physisorption depends on the strength of the van der Waals interaction between the adsorbate and the adsorbent, the capacity in this method strongly depends on the nature of the porous support. In addition, it should be better to have large surface area, pore volume, appropriate pore size, and low density. In this respect, porous metallosupramolecular networks must be good candidates for hydrogen storage materials. Since Yaghi et al. have carried out experiments of H_2 adsorption with metallosupramolecular networks in 2003, various metallosupramolecular networks have been reported as the hydrogen storage materials [42,64,65,84,85–88]. Extensive reviews have been made on the hydrogen storage by the metallosupramolecular networks [89,90]. Hydrogen storage capacities of typical metallosupramolecular networks are summarized in Table 3.

Table 3
Hydrogen storage properties of metallosupramolecular networks[a]

Formula or name	H_2 uptake (wt%)	Condition	Reference
IRMOF-1	4.5	78 K, 0.8 bar	[89]
	0.5[a]	RT, 10 bar	[89]
	1.0	RT, 20 bar	[89]
	1.32	77 K, 1 atm	[65]
IRMOF-6	1.0[a]	RT, 10 bar	[89]
IRMOF-8	2.0	RT, 10 bar	[89]
	1.50	77 K, 1 atm	[65]
IRMOF-11	1.62	77 K, 1 atm	[65]
IRMOF-18	0.89	77 K, 1 atm	[65]
MOF-177	1.25	77 K, 1 atm	[65]
[Cu(hfipbb)(H_2hfipbb)$_{0.5}$] (**3**-**13**)	~1	RT, 48 atm	[75]
MOF-505	2.48	77 K, 1 atm	[84]
MIL-100	3.28	77 K, 2.65 MPa	[85]
	0.15	RT, 7.33 MPa	[85]
MIL-101	6.1	77 K, 8 MPa	[85]
	0.43	RT, 8 MPa	[85]
MIL-53 (Al)	3.8	77 K, 16 bar	[91]
MIL-53 (Cr)	3.1	77 K, 16 bar	[91]
$Zn_4O(NTB)_2$ (**1**-**2**′)	1.9	77 K, 1 atm	[36]
$Zn_3(NTB)_2$ (**1**-**3**′)	1.0	77 K, 1 atm	[37]
Mn(NDC) (**1**-**1**′)	0.57	77 K, 1 atm	[33]
[Ni(L)][bpydc] (**2**-**2**′)	1.1	77 K, 1 atm	[48]
[Ni(L_{me})][bpdc] (**2**-**3**′)	0.7	77 K, 1 atm	[54]
$Mn(H_2CO_2)_2$ (**3**-**12**′)	0.9	78 K, 1 atm	[92]
Zn_2(ABTC)$(DMF)_2$	2.07	77 K, 1 atm	[93]
Cu_2(ABTC)	2.87	77 K, 1 atm	[93]

[a] Estimated from the formula weight and the reported sorption data.

4. Selective guest binding

Porous metallosupramolecular networks capable of selective sorption of certain guest molecules are useful in sensing and separation of the guest molecules. Suh and co-workers reported various networks that exhibited selective binding of guest molecules such as D-glucose [15], metal complexes [14], alcohols, and organic compounds [12,13,16,36,48,49]. The guest molecules are recognized by the cavities of the networks due to the host–guest interactions such as hydrogen bonds and/or π–π interactions.

A 3D network $\{[Ni(L)(H_2O)_2]_3[BTC]_2\}_n \cdot 24nH_2O$ (**2**-**6**, L = 1,4,8,11-tetraazacyclotetradecane) assembled from $[Ni(L)]^{2+}$ and BTC^{3-} in water generates 1D channels (Fig. 34) [15]. The host solid selectively binds D-glucose into the channels over maltose, a dimer of glucose, due to the size effect of the channels (aperture size, 10.3 Å).

In addition to the size effect, host–guest interactions are also important for the selective binding of the guest. For example, $\{[Ni(L)]_3[BTC]_2\}_n \cdot 18nH_2O$ (**2**-**7**), which was assembled from Ni(II) hexaazamacrocycle $[Ni(L)]^{2+}$ and BTC^{3-} in DMF/H_2O

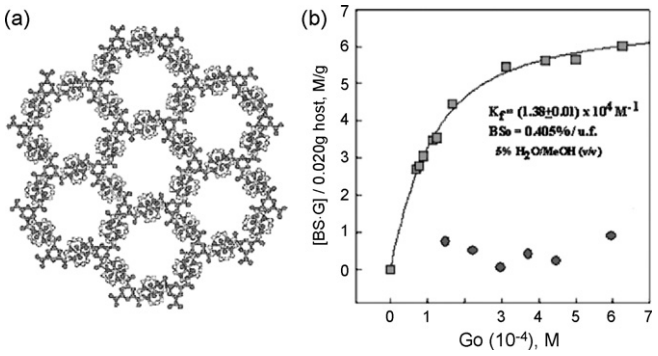

Fig. 34. (a) View showing honeycomb channels of **2-6**. Water molecules included in the channels are omitted for clarity. (b) Binding of **2-6** with D-glucose (square) and maltose (circle), respectively. Reproduced with permission from Ref. [15].

to generate 1D channels, binds selectively PhOH over PhCl and PhBr because of the hydrogen bonding interactions between the host and guest (Fig. 35) [49].

Suh and co-workers reported $\{[Cu(L_{me})]_3[BTC]_2\}_n \cdot 18nH_2O$ (**2-8**, L_{me} = 3,10-dimethyl-1,3,5,8,10,12-hexaazacyclotetradecane), in which 1D honeycomb channels are generated [16]. The solid **2-8** bound guest molecules in the order of EtOH > MeOH > PhOH [16]. However, the measured total volume (1533 $Å^3$) of PhOH molecules included in the formula unit of the host was much greater than the void volume (566 $Å^3$) of the host, indicating that phenol guests must be intercalated between the host layers instead of being included in the channels (Fig. 36).

Suh et al. reported that the dried solid of pillared bilayer network **2-11′** is able to differentiate MeOH, EtOH, isopropyl alcohol, and benzyl alcohol in toluene medium (Fig. 37) [11,12]. As for the binding constant, the host binds the guests in the order of benzyl alcohol > isopropyl alcohol > MeOH ~ EtOH. The reason why the host binds benzyl alcohol the best is that the phenyl rings of benzyl alcohol interact with xylyl pillars of the host via π–π interactions. The inclusion capacity (in mol) is in the order of MeOH > EtOH > isopropyl alcohol > benzyl alcohol.

The network generating 1D channels, $\{[Ni(L)](bpydc)\}_n$ (**2-2′**) binds guests in the order EtOH ≈ PhOH > pyridine > benzene, while it does not bind toluene [48]. The host favors guests that can form hydrogen bonds with its carbonyl groups, which are exposed to the channels (Fig. 38).

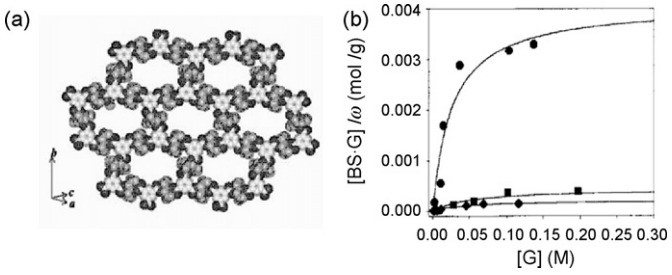

Fig. 35. (a) CPK representation of **2-7**. (b) Binding of **2-7** with PhOH (●), PhBr (■), and PhCl (♦) in *n*-hexane medium. Reproduced with permission from Ref. [49].

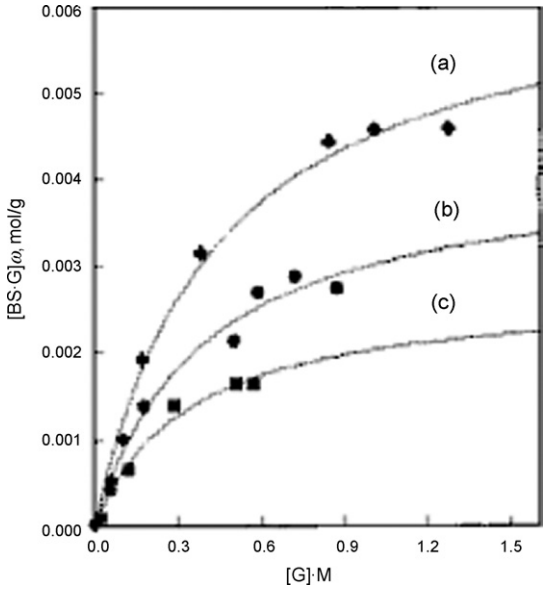

Fig. 36. Binding of host solid **2-8** with organic guest: PhOH (□); MeOH (●); EtOH (■). Reproduced with permission from Ref. [16].

In addition, pyridine molecules are bound to the host better than benzene because of the Lewis base–π interactions.

The network solid $[Zn_4O(NTB)_2]$ (**1-2′**) is able to differentiate MeOH, pyridine, benzene, and dodecane in the isooctane medium [36]. The K_f values for the formation of host–guest compounds are in the order of MeOH > pyridine > benzene > dodecane. These phenomena indicate that the host favors the guests that are able to form hydrogen bonds with its carbonyl groups exposed to the channels. In addition, it favors the hydrophobic guests because of the benzyl rings contained in the host that might induce π–π or C–H···π interactions with the guest molecules (Fig. 39).

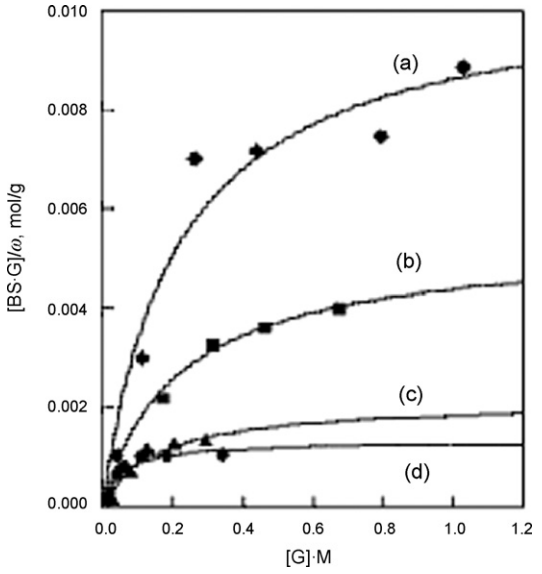

Fig. 37. Binding of host **2-11** with the organic guests: (a) MeOH (●); (b) EtOH (▼); (c) *iso*-PrOH (■); (d) BzOH (□) in toluene medium. Reproduced with permission from Ref. [12].

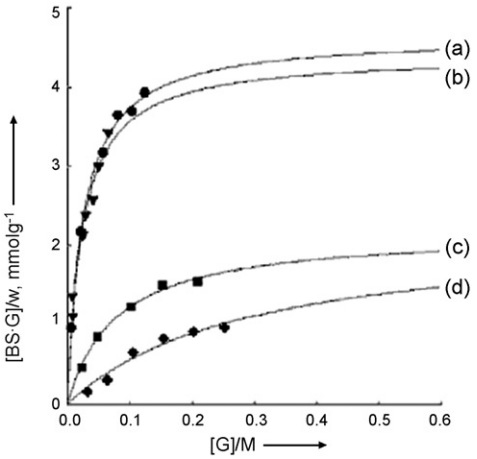

Fig. 38. Binding of host **2**-**2** with the organic guests: (a) EtOH (●); (b) PhOH (▼); (c) pyridine (■); (d) benzene (♦). Reproduced with permission from Ref. [48].

5. Low dimensional alignment of guest molecules

The 1D array of atoms or molecules, which show properties of conducting charge or photonic energy, are regarded as the major components of future devices based on molecular sized functional units [94]. Furthermore, the confinement of atoms and molecules into low dimensional nano space may show different properties and reactivity from the bulk materials. Some supramolecular networks have been utilized to align atoms and molecules [95–99].

Hulliger and co-workers presented the chainlike alignment of I_2 molecules, surrounded by a π-donor-type environment of TPP (tris-(*o*-phenylenedioxy) cyclotriphosphazene) host (**5**-**1**) (Fig. 40) [95]. This organic zeolite crystals, in which trigonal arrangement of phosphazene molecules provided a hexagonal channel structures, efficiently adsorbed I_2 vapor and resulted in TPP·*x*(THF)·*y*(I_2), wherein iodine formed molecular chains. The aligned iodine chains in TPP channels showed the electrical

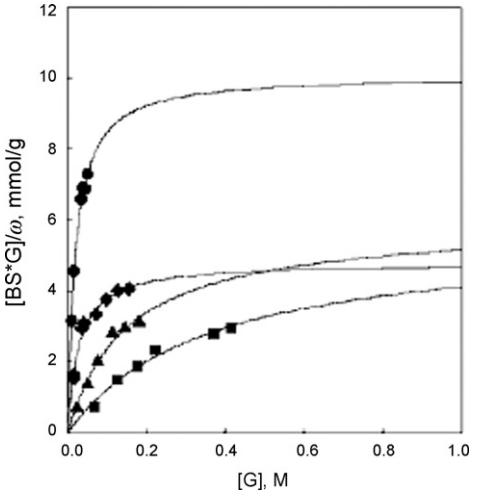

Fig. 39. Binding of host solid **1**-**2**′ with organic guests: MeOH (●), pyridine (♦), benzene (▲), and dodecane (■). Reproduced with permission from Ref. [36].

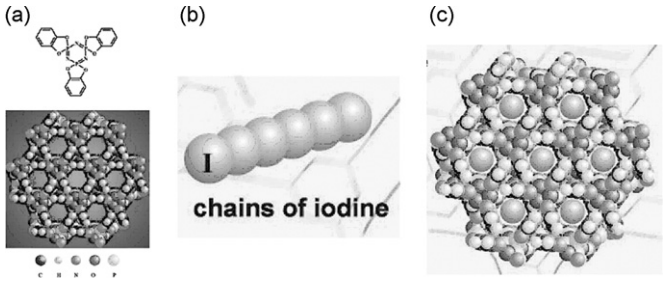

Fig. 40. (a) Molecular structure of TPP and the channel topology. (b) Proposed structure showing the chains of iodine. (c) The chains of iodine aligned in the hexagonal channel of TPP. Reproduced with permission from Ref. [95].

conductivity of 10^{-6} to $10^{-8}\ \Omega^{-1}\ m^{-1}$ at 25 °C for a potential of 50 V.

Kim and co-workers reported an ultra thin silver wire with 0.4 nm width grown up inside the pores of self-assembled calix[4]hydroquinone (CHQ) nanotubes (**5**-**2**) [96]. The 1D structure of silver nanowire formed in CHQ crystals, which was prepared by UV irradiation at an ambient temperature in the aqueous phase, was unidirectional and monodispersed due to the self-assembled CHQ nanotube arrays (Fig. 41).

Kitagawa and co-workers reported the dioxygen molecular arrays that were physisorbed in the nanochannels of a microporous copper network $\{Cu_2(pzdc)_2(pyr)\}_n$ (**5**-**3**), which had a pillared layer structure with 1D channels of aperture size 4.0 Å × 6.0 Å. The O_2 confinement in the host structure was characterized by the MEM (maximum entropy method)/Rietveld method based on in situ high-resolution synchrotron X-ray powder diffraction data [97]. The O_2 molecules were found in the middle of the channels of **5**-**3** under the condition of 80 kPa at 90 K (Fig. 42). The confinement effect and the restricted geometry of 1D nanochannels lead to a 1D ladder-like structure of O_2 dimer. The O_2 molecules adsorbed in the nanochannels were similar to the solid state rather than the liquid state at 90 K, which is much higher than the freezing point (54.4 K) of O_2 under atmospheric pressure.

Takamizawa et al. also reported the direct observation of dioxygen molecular chains, which were aligned inside the crystal of $[Rh_2^{II}(bza)_4(pyz)]_n$ (**5**-**4**) (bza = benzoate, pyz = pyrazine) at 90 K [98].

Kitagawa and co-workers also reported the alignment of acetylene molecules in the channels of $[Cu_2(pzdc)_2(pyz)]$ (**5**-**3**) (pzdc = pyrazine-2,3-dicarboxylate, pyz = pyrazine) at 170 K.

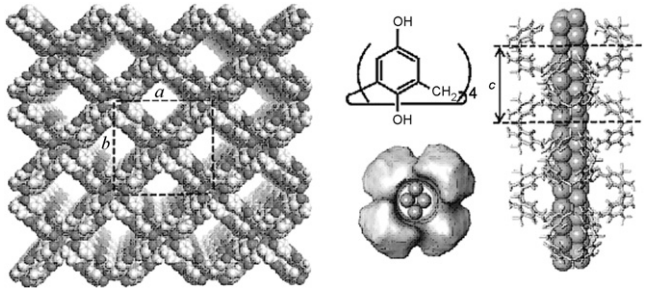

Fig. 41. CHQ nanotube templates and a silver nanowire inside the nanotube. Reproduced with permission from Ref. [96].

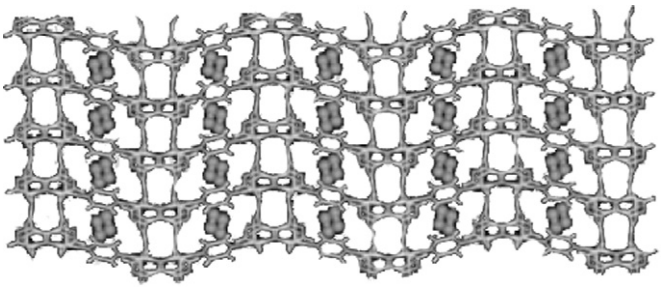

Fig. 42. Views down from the *b*- and *c*-axis, respectively. Reproduced with permission from Ref. [97].

They characterized it by using MEM/Rietveld analysis for the powder X-ray diffraction data [99]. In the channels, the C_2H_2 molecules align along the *a*-axis, with an inclination of 78.1° with the intermolecular distance of 4.8 Å. They are densely packed with a short intermolecular distance while avoiding the close contact that induces an explosion. The interaction between the hydrogen atoms of C_2H_2 and the non-coordinating oxygen atoms of the host is based not only on electrostatic attraction but also on the electron delocalization effect between H and O atoms. These interactions strongly fix the C_2H_2 in the 1D channels, which gives rise to the enhancement of the 'confinement effect' and enables the stable accommodation of C_2H_2 molecules (Fig. 43).

Suh and co-workers reported that the hexagonal water columns were formed by the hydrogen-bonding interactions between the guest water molecules contained in the 1D honeycomb channels of $\{[Cu(L_{me})]_3[BTC]_2\}_n \cdot 18nH_2O$ (**2-8**) (Fig. 44) [16]. When the host was assembled in the presence of phenol, highly ordered PhOH layer was constructed, which was packed alternately with the host layers. The phenol molecules are included in the host network such that the benzene ring planes lie almost perpendicularly to the network and the hydroxyl groups of the phenol guests are hydrogen-bonded with the host. Phenol molecules are linked together by the edge-to-face π–π interactions, which generates a highly ordered 2D noncovalent phenol network (Fig. 44). The 2D phenol network forms honeycomb-like cavities, each of which consists of 12 phenol molecules, 6 locating at the corners of the hexagon with ring planes directing toward inside of the cavity and 6 locating on the side of the hexagon by being shared with the adjacent rings.

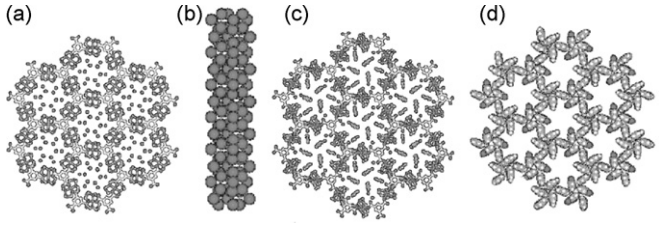

Fig. 44. (a) X-ray structure of **2-8**, showing 1D channels created perpendicularly to the *ab* plane. (b) Water column created in each channel of **2-8**. (c) X-ray structure of **2-8′** (view of the *ab* plane). (d) View of noncovalent phenol network in **2-8′**. Reproduced with permission from Ref. [16].

6. Solid state sensors

The metallosupramolecular networks that have luminescence properties together with size- or shape-selective sorption properties can be applied in sensor devices. Luminescent networks would be prepared by utilizing luminescent organic building blocks [36,100] and/or luminescent metal building blocks [25,101], or by utilizing the ligand-to-metal charge transfer [102–104]. However, the assembly of transition metals and luminescent ligands frequently results in luminescence-quenched networks [51]. In some cases, even though the metallosupramolecular networks have luminescent properties, the networks are not porous enough to show inclusion behavior. A few networks exhibited the guest dependent luminescence [36,105,106]. The presence of lanthanide centers can provide luminescence.

Suh and co-workers reported $[Zn_4O(NTB)_2]_n \cdot 3nDEF\cdot n$EtOH (**1-2**) and its desolvated solid $[Zn_4O(NTB)_2]_n$ (**1-2′**), which exhibit guest dependent photoluminescence [36]. The network solids **1-2** and its guest removed solid **1-2′** show photoluminescence maxima at $\lambda_{max} = 433$ nm and $\lambda_{max} = 463$ nm, respectively, upon photoexcitation at 340 nm (Fig. 45(a)). The 30 nm difference in the luminescence spectra between **1-2** and **1-2′** is attributed to the absence and presence of π–π interactions, respectively, between the interpenetrated nets of the host. The luminescence also depends on the guest identity

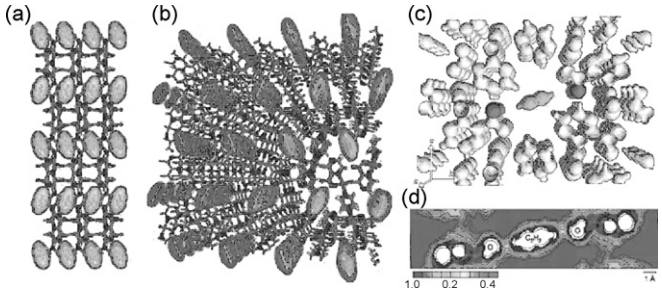

Fig. 43. (a) The host solid **5-3** with adsorbed C_2H_2 seen down the *c*-axis. (b) Perspective view down the *a*-axis. (c) MEM electron densities of C_2H_2 adsorbed host at 170 K as an equal-density contour surface along the *a*-axis. (d) MEM electron density distribution views on the 2D section defined by the molecular axis of the C_2H_2 molecule and the *a*-axis. Reproduced with permission from Ref. [99].

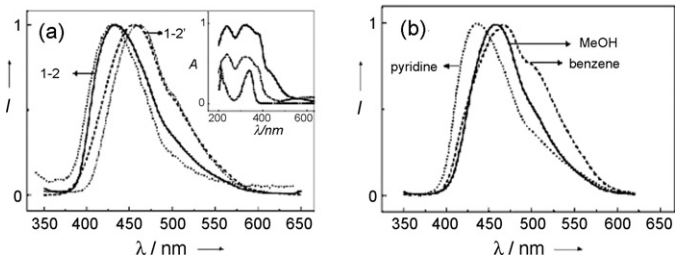

Fig. 45. (a) Luminescent spectra: **1-2** (—), **1-2′** (·····), solid Na_3NTB (···), and the 0.1 M NaOH solution of H_3NTB (- - -). (Inset) Absorption spectra of **1-2** (—, $\lambda_{max} = 237$, 321, 375(sh), and 428(sh) nm), solid Na_3NTB (···, $\lambda_{max} = 237$, 321, and 375(sh) nm), and the 0.1 M NaOH solution of H_3NTB (- - -, $\lambda_{max} = 340$ nm). (b) Guest-dependent luminescent spectra with normalized intensity: pyridine (···, $\lambda_{max} = 435$ nm), methanol (—, $\lambda_{max} = 456$ nm), and benzene (- - -, $\lambda_{max} = 466$ nm). Reproduced with permission from Ref. [36].

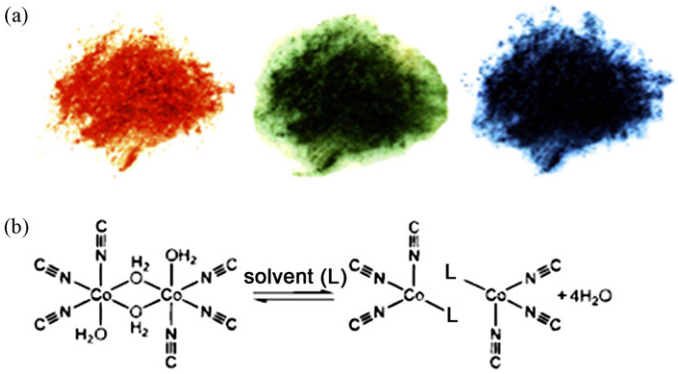

Fig. 46. (a) Pictures showing apparent color changes of **6-3**. Orange (water) as prepared, green (THF), and blue (diethyl ether). (b) Proposed model for the vapor-chromic responses of **6-2** and **6-3** networks. Reproduced with permission from Ref. [26].

(Fig. 45(b)). When desolvated solid **1-2′** was immersed in the solvents such as pyridine, methanol, and benzene, λ_{max} of the luminescence appears at 435 nm, 456 nm, and 466 nm, respectively. The guest-dependent luminescence shows no relationship with the binding constant of the host with the guest. Therefore, this solid material can be applied as a sensor for organic molecules.

Yaghi and co-workers reported the blue luminescent 3D network $[Tb_2(BDC)_3(H_2O)_4]_n$ (**6-1**) [105]. On thermal dehydration, **6-1** was changed to a microporous material having 1D channels, $[Tb_2(BDC)_3]$ (**6-1′**). **6-1′** contains accessible metal sites in its channels, and adsorbs water and ammonia. The network showed different luminescence spectra depending on the presence or absence of guest molecules as well as the type of guest molecules, which could be potential luminescent probes for the assay of small molecules.

Long et al. reported porous metallosupramolecular networks, which displayed dramatic color changes upon exposure to certain organic solvents. $[Co_2(H_2O)_4][Re_6S_8(CN)_6]\cdot 10H_2O$ (**6-2**) and $[Co(H_2O)_3]_4[Co_2(H_2O)_4][Re_6Se_8(CN)_6]_3\cdot 44H_2O$ (**6-3**) were assembled from face-capped octahedral clusters of the type $[Re_6Q_8(CN)_6]^{4-}$ (Q = S, Se) and hydrated Co^{2+} ions (Fig. 46) [26]. The color change was explained by that solvent molecules entering the cavities and channels in the networks displaced solvate water molecules, thereby disrupting the hydrogen-bonded network supporting the $[Co_2(H_2O)_4]^{4+}$ clusters. Labile water ligands are then released from the destabilized octahedral $Co(NC)_3(H_2O)_3$ centers, leaving a pair of disconnected $Co(NC)_3(L)$ moieties to relax into tetrahedral configurations. The noncyanide ligand (L) could either be a lingering water molecule or a solvent molecule, depending on the coordinating ability and the steric requirements of the incoming solvent. The color of the compounds in response to a given solvent is therefore determined by how far to the right it pushes the following equilibrium.

Chen et al. reported microporous network $[Eu(BTC)(H_2O)]\cdot 1.5H_2O$ (**6-4**) (BTC = benzenetricarboxylate) [25]. There exist 1D channels of 6.6 Å × 6.6 Å along the *c*-axis, which are filled with coordinating and free water molecules. The emission spectrum of Eu(BTC) (**6-4′**) excited at 285 nm indicates that

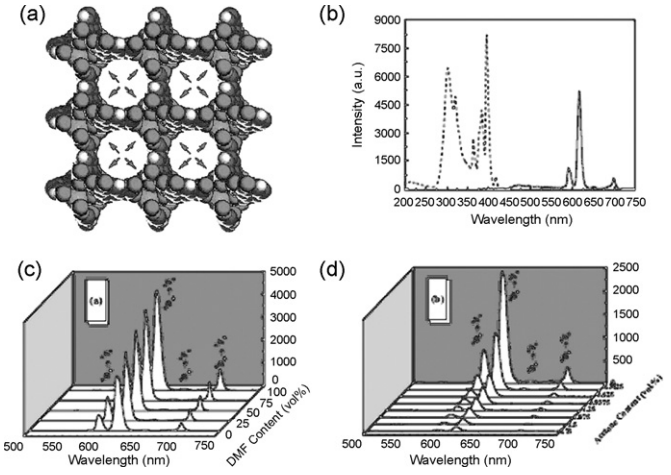

Fig. 47. (a) X-ray structure of **6-4**. (b) The excitation (dotted line) and PL spectrum (solid line) of solid of **6-4′**. The PL spectra in the presence of various content of (c) DMF and (d) acetone solvent, respectively (excited at 285 nm). Reproduced with permission from Ref. [25].

the characteristic emission from BTC ligands around 380 nm disappears, and that there exists energy transfer from BTC ligands to Eu^{3+} ions that "magnifies" the luminescence of the f–f transitions. The potential of **6-4′** to be the sensing material of small molecules was revealed by it is fluorescence properties in different solvent emulsions. DMF and acetone exhibit the most significant enhancing and quenching effects, respectively. The fluorescence intensity gradually increases with the addition of DMF solvent, while decreases with the addition of acetone solvent. These phenomena are attributed to the binding interaction of the luminescent open metal sites with guest solvent molecules (Fig. 47) [25].

Wong et al. reported a lanthanide network $\{[Tb(Mucicate)_{1.5}(H_2O)_2]\cdot 5H_2O\}_n$ (**6-5**), which generates 1D channels. The network acts as a luminescent receptor for reversible selective anion monitoring. In the hydration state of the host, f–f luminescent properties are quenched due to vibrational quenching of water molecules, while the emission intensity is enhanced upon removal of water molecules. Upon addition of an aqueous solution of sodium salts of I^-, Br^-, Cl^-, F^-, CN^-, and CO_3^{2-} to a solid sample of the host at various time points, the emission intensity was increased. However, the intensity is independent of the cation such as the Na^+, K^+, and Ca^{2+} [107].

7. Conclusions

A large number of porous metallosupramolecular networks have been reported. They have been prepared by the solvothermal reactions or by the molecular self-assembly at ambient temperature by using metal and organic building blocks. The porous networks thus prepared have pores or channels of various shapes and sizes with characteristic chemical environments, which offer different binding abilities and capacities with different guest molecules. The networks as synthesized contain guest solvent molecules in the pores and channels. If the networks adsorb significant amount of gases on removal of the guest

molecules to show porosity, they can be applied in gas storage and gas separation processes. In particular, hydrogen storage and carbon dioxide sequestration are the major concerns of the chemists involving in metallosupramolecular chemistry.

The metallosupramolecular networks are able to bind organic guests with different binding constants and capacities, and thus can be applied in separation of organic molecules [12–16,36,48,49]. Some metallosupramolecular network solids are practically applied in GC column materials to separate organic compounds [76,77]. The metallosupramolecular networks also bind metal complexes selectively [14], which can be applied in environmental purification.

The network properties sometimes are changed by inclusion and removal of guest molecules. The cooperative properties between networks and guest molecules would generate unprecedented properties of the metallosupramolecular networks, such as absorption spectra, luminescence properties, and magnetic properties, which must be the major concern of the chemists.

Another exciting and underdeveloped area is the design and synthesis of the redox-active metallosupramolecular networks, where oxidation and reduction of the overall framework can be induced by the guest molecules without overall decomposition of the network. If a neutral network is oxidized, it would include free counter anions in the channels or pore, and the resulting network could be applied as the anion-exchange materials [12]. In this case, the other properties such as magnetism and conductivity might be also affected by the redox reactions between the host solid and the included guest. Recently, redox active metallosupramolecular networks have been employed for the fabrication of monodispersed and small (<5 nm) metal nanoparticles such as gold, silver, and palladium nanoparticles, which have been known to be very difficult to fabricate, simply by immersion of the network solid in the metal ion solutions [54,55,79]. In this regard, metallosupramolecular networks are expected to be used as the matrixes for fabricating nanoparticles or nanowires of various metals, and the nanocomposite materials thus formed may be used as efficient catalysts in various reactions.

Other important property of the porous metallosupramolecular networks is the molecular dynamics occurring within the single crystal in response to the external stimuli. The phenomena are referred to single-crystal to single-crystal transformations [11,12,36,37,55,56,72,76,108] and they are very important for the development of the crystalline devices and sensors.

In short, well-designed metallosupramoelcular networks have great potentials to be applied in storage and separation of gases and organic molecules, sensing of organic and inorganic molecules, ion-exchange, catalysis, and matrixes for fabrication of metal nanoparticles.

Acknowledgments

This work was supported by the Korea Research Foundation Grant funded by the Korean Government (MOEHRD, Basic Research Promotion Fund) (KRF-2005-084-C00020) and by the SRC program of MOST/KOSEF through the Center for Intelligent Nano-Bio Materials (Grant no. R11-2005-008-00000-0).

References

[1] J.M. Lehn, Supramolecular Chemistry: Concepts and Perspectives, VCH, Weinheim, 1995.
[2] J.W. Steed, J.L. Atwood, Supramolecular Chemistry, John Wiley & Sons, Chichester, 2002.
[3] J. Lewinski, J. Zachara, I. Justyniak, M. Dranka, Coord. Chem. Rev. 249 (2005) 1185.
[4] M.P. Suh, K.S. Min, J.W. Ko, H.J. Choi, Eur. J. Inorg. Chem. (2003) 1373.
[5] X. Shi, G. Zhu, X. Wang, G. Li, Q. Fang, G. Wu, G. Tian, M. Xue, X. Zhao, R. Wang, S. Qiu, Cryst. Growth Des. 5 (2005) 207.
[6] H.W. Roesky, M. Andruh, Coord. Chem. Rev. 236 (2003) 91.
[7] J.T. Lenthall, J.W. Steed, Coord. Chem. Rev. 251 (2007) 1747.
[8] D. Bradshaw, J.B. Claridge, E.J. Cussen, T.J. Prior, M.J. Rosseinsky, Acc. Chem. Rev. 38 (2005) 273.
[9] (a) G.S. Papaefstathiou, L.R. MacGillivray, Coord. Chem. Rev. 246 (2003) 169;
(b) B. Moulton, M.J. Zaworotko, Chem. Rev. 101 (2001) 1629.
[10] G.R. Desiraju, Angew. Chem. Int. Ed. 46 (2007) 8342.
[11] M.P. Suh, J.W. Ko, H.J. Choi, J. Am. Chem. Soc. 124 (2002) 10976.
[12] H.J. Choi, M.P. Suh, J. Am. Chem. Soc. 126 (2004) 15844.
[13] H. Kim, M.P. Suh, Inorg. Chem. 44 (2005) 810.
[14] K.S. Min, M.P. Suh, Chem. Eur. J. 7 (2001) 303.
[15] H.J. Choi, T.S. Lee, M.P. Suh, Angew. Chem. Int. Ed. 38 (1999) 1405.
[16] J.W. Ko, K.S. Min, M.P. Suh, Inorg. Chem. 41 (2002) 2151.
[17] M. Eddaoudi, H. Li, O.M. Yaghi, J. Am. Chem. Soc. 122 (2000) 1391.
[18] K.S. Min, M.P. Suh, J. Am. Chem. Soc. 122 (2000) 6834.
[19] H.J. Choi, M.P. Suh, Inorg. Chem. 42 (2003) 1151.
[20] Y. Liu, G. Li, X. Li, Y. Cui, Angew. Chem. Int. Ed. 46 (2007) 6301.
[21] C.D. Wu, A. Hu, L. Zhang, W. Lin, J. Am. Chem. Soc. 127 (2005)8940.
[22] (a) T. Uemura, R. Kitaura, Y. Ohta, M. Nagaoka, S. Kitagawa, Angew. Chem. Int. Ed. 45 (2006) 4112;
(b) T. Uemura, S. Horike, S. Kitagawa, Chem. Asian J. 1 (2006) 36;
(c) T. Uemura, D. Hiramatsu, Y. Kubota, M. Takata, S. Kitagawa, Angew. Chem. Int. Ed. 46 (2007) 4987.
[23] B. Gomez-Lor, E. Gutierrez-Puebla, M. Iglesias, M.A. Monge, C. Ruiz-Valero, N. Snejko, Chem. Mater. 17 (2005) 2568.
[24] C.A. Bauer, T.V. Timofeeva, T.B. Settersten, B.D. Patterson, V.H. Liu, B.A. Simmons, M.D. Allendorf, J. Am. Chem. Soc. 129 (2007) 7136.
[25] B. Chen, Y. Yang, F. Zapata, G. Lin, G. Qian, E.B. Lobkovsky, Adv. Mater. 19 (2007) 1693.
[26] W.J. Rister, K.M.L. Taylor, W. Lin, J. Am. Chem. Soc. 129 (2007) 9852.
[27] O.R. Evans, W. Lin, Chem. Mater. 13 (2001) 2705.
[28] M. O'Keeffe, M. Eddaoudi, H. Li, T.M. Reineke, O.M. Yaghi, Solid State Chem. 152 (2000) 3.
[29] M. O'Keeffe, B.G. Hyde, Crystal Structures. I. Patterns and Symmetry, Mineralogical Society of America, Washington, DC, 1996.
[30] S.R. Batten, R. Robson, Angew. Chem. Int. Ed. 37 (1998) 1460.
[31] O.M. Yaghi, M. O'Keeffe, N.W. Ockwig, H.K. Chae, M. Eddaoudi, J. Kim, Nature 423 (2003) 705.
[32] M. Eddaoudi, J. Kim, N. Rosi, D. Vodak, J. Wachter, M. O'keeffe, O.M. Yaghi, Science 295 (2002) 469.
[33] H.R. Moon, N. Kobayashi, M.P. Suh, Inorg. Chem. 45 (2005) 8672.
[34] M. Dinca, J.R. Long, J. Am. Chem. Soc. 127 (2005) 9376.
[35] K.O. Kongshaug, H. Fjellvag, Solid State Sci. 5 (2003) 303.
[36] E.Y. Lee, S.Y. Jang, M.P. Suh, J. Am. Chem. Soc. 127 (2005) 6374.
[37] M.P. Suh, Y.E. Cheon, E.Y. Lee, Chem. Eur. J. 13 (2007) 4208.
[38] J.L.C. Rowsell, O.M. Yaghi, Micropor. Mesopor. Mater. 73 (2004) 3.
[39] N.L. Rosi, M. Eddaoudi, J. Kim, M. O'Keeffe, O.M. Yaghi, Angew. Chem. Int. Ed. 41 (2002) 284.
[40] B. Chen, M. Eddaoudi, S.T. Hyde, M. O'Keeffe, O.M. Yaghi, Science 291 (2001) 1021.
[41] B. Kesanli, Y. Cui, M.R. Smith, E.W. Bittner, C. Bockrath, W. Lin, Angew. Chem. Int. Ed. 44 (2005) 72.
[42] D. Sun, S. Ma, Y. Ke, D.J. Collins, H.-C. Zhou, J. Am. Chem. Soc. 128 (2006) 3896.
[43] S. Ma, D. Sun, M. Ambrogio, J.A. Fillinger, S. Parkin, H.-C. Zhou, J. Am. Chem. Soc. 129 (2007) 1858.

[44] K. Yamada, S. Yagishita, H. Tanaka, K. Tohyama, K. Adachi, S. Kaizaki, H. Kumagai, K. Inoue, R. Kitaura, H.C. Chang, S. Kitagawa, S. Kawata, Chem. Eur. J. 10 (2004) 2547.
[45] S. Masaoka, D. Tanaka, Y. Malanishi, S. Kitagawa, Angew. Chem. Int. Ed. 43 (2004) 2530.
[46] B. Chen, N.W. Ockwig, F.R. Fronczek, D.S. Contreras, O.M. Yaghi, Inorg. Chem. 44 (2005) 181.
[47] M.P. Suh, H.R. Moon, Adv. Inorg. Chem. 59 (2007) 39.
[48] E.Y. Lee, M.P. Suh, Angew. Chem. Int. Ed. 43 (2004) 2798.
[49] H.J. Choi, T.S. Lee, M.P. Suh, J. Incl. Phenom. Macrocycl. Chem. 41 (2001) 155.
[50] H.J. Choi, M.P. Suh, J. Am. Chem. Soc. 120 (1998) 10622.
[51] M.P. Suh, H.J. Choi, S.M. So, B.M. Kim, Inorg. Chem. 42 (2003) 676.
[52] H.J. Choi, M.P. Suh, Inorg. Chem. 38 (1999) 6309.
[53] K.S. Min, M.P. Suh, Eur. J. Inorg. Chem. (2001) 449.
[54] H.R. Moon, J.H. Kim, M.P. Suh, Angew. Chem. Int. Ed. 44 (2005) 1261.
[55] M.P. Suh, H.R. Moon, E.Y. Lee, S.Y. Jang, J. Am. Chem. Soc. 128 (2006) 4710.
[56] M.P. Suh, Y.E. Cheon, Aust. J. Chem. 59 (2006) 605.
[57] (a) S. Lidin, M. Jacob, S. Anderson, J. Solid State Chem. 114 (1995) 36; (b) N.L. Rosi, J. Kim, M. Eddaoudi, B. Chen, M. O'Keeffe, O.M. Yaghi, J. Am. Chem. Soc. 127 (2005) 1504.
[58] R. Kitaura, K. Seki, G. Akiyama, S. Kitagawa, Angew. Chem. Int. Ed. 42 (2003) 428.
[59] S. Kitagawa, R. Kitaura, S. Noro, Angew. Chem. Int. Ed. 43 (2004) 2334.
[60] K. Uemura, R. Matsuda, S. Kitagawa, J. Solid State Chem. 178 (2005) 2420.
[61] K.S.W. Sing, D.H. Everett, R.A.W. Haul, L. Moscou, R.A. Pierotti, J. Rouquerol, T. Siemieniewska, Pure Appl. Chem. 57 (1985) 603.
[62] F. Rouquerol, J. Rouquerol, K. Sing, Adsorption by Powders and Porous Solids, Academic Press, London, 1999.
[63] H. Li, M. Eddaoudi, M. O'Keeffe, O.M. Yaghi, Nature 402 (1999) 276.
[64] G. Ferey, C. Mellot-Draznieks, C. Serre, F. Millange, J. Cutour, S. Surble, I. Margiolaki, Science 309 (2005) 2040.
[65] G. Ferey, C. Serre, C. Mellot-Draznieks, F. Millange, S. Surble, J. Dutour, I. Margiolaki, Angew. Chem. Int. Ed. 43 (2004) 6296.
[66] X. Lin, J. Jia, X. Zhao, K.M. Thomas, A.J. Blake, G.S. Walker, N.R. Champness, P. Hubberstey, M. Schröder, Angew. Chem. Int. Ed. 45 (2006) 7358.
[67] H.K. Chae, D.Y. Siberio-Perez, J. Kim, Y. Go, M. Eddaoudi, A.J. Matzger, M. O'Keeffe, O.M. Yaghi, Nature 427 (2004) 523.
[68] B. Chen, N.W. Ockwig, A.R. Millward, D.S. Contreras, O.M. Yaghi, Angew. Chem. Int. Ed. 46 (2005) 4745.
[69] J.L.C. Roswell, O.M. Yaghi, J. Am. Chem. Soc. 128 (2006) 1304.
[70] S. Surble, F. Millange, C. Serre, T. Duren, M. Latroche, S. Bourrelly, P.L. Llewellyn, G. Ferey, J. Am. Chem. Soc. 128 (2006) 14889.
[71] K. Uemura, S. Kitagawa, K. Fukui, K. Saito, J. Am. Chem. Soc. 126 (2004) 3817.
[72] T.K. Maji, G. Mostafa, R. Matsuda, S. Kitagawa, J. Am. Chem. Soc. 127 (2005) 17152.
[73] L. Pan, K.M. Adams, H.E. Hernandez, X. Wang, C. Zheng, Y. Hattori, K. Kaneko, J. Am. Chem. Soc. 125 (2003) 3062.
[74] S. Ma, D. Sun, X.-S. Wang, H.-C. Zhou, Angew. Chem. Int. Ed. 46 (2007) 2458.
[75] L. Pan, D.H. Olson, L.R. Ciemnolonski, R. Heddy, J. Li, Angew. Chem. Int. Ed. 45 (2006) 616.
[76] B. Chen, C. Liang, J. Yang, D.S. Contreras, Y.L. Clancy, E.B. Lobkovsky, O.M. Yaghi, S. Dai, Angew. Chem. Int. Ed. 45 (2006) 1390.
[77] L.A. Christine, E.A. Kirschhock, M. Maes, M.A. van der Veen, V. Finsy, A. Depla, J.A. Martens, G.V. Baron, P.A. Jacobs, J.F.M. Denayer, D.E. De Vos, Angew. Chem. Int. Ed. 46 (2007) 4293.
[78] D.W. Breck, Zeolite Molecular Sieves, Wiley & Sons, New York, 1974.
[79] Y.E. Cheon, M.P. Suh, Chem. Eur. J. (2008), in press.
[80] R.N. Devi, M. Edgar, J. Gonzalex, A.M. Slawin, D.P. Tunstall, P. Grewal, P.A. Cox, P.A. Wright, J. Phys. Chem. B 108 (2004) 535.
[81] L. Schlapbach, A. Zuttel, Nature 414 (2001) 353.
[82] P. Berinstein, Alternative Energy: Facts, Statistics, and Issues, vol. A72, Oryx Press, 2001, p. 619.
[83] M.G. Nijkamp, J.E.M.J. Raaymakers, A.J. van Dillen, K.P. de Jong, Appl. Phys. 126 (2001) 5666.
[84] J.L.C. Rowsell, A.R. Millward, K.S. Park, O.M. Yaghi, J. Am. Chem. Soc. 126 (2004) 5666.
[85] M. Latroche, S. Surble, C. Serre, C. Mellot-Draznieks, P.L. Llewellyn, J.-H. Lee, J.-S. Chang, S.H. Jhung, G. Ferey, Angew. Chem. Int. Ed. 45 (2006) 8227.
[86] A.G. Wong-Foy, A.J. Matzger, O.M. Yaghi, J. Am. Chem. Soc. 128 (2006) 3494.
[87] Y. Li, R.T. Yang, J. Am. Chem. Soc. 128 (2006) 8136.
[88] N.L. Rosi, J. Eckert, M. Eddaoudi, D.T. Vodak, J. Kim, M. O'Keeffe, O.M. Yaghi, Science 300 (2003) 1127.
[89] J.L.C. Rowsell, O.M. Yaghi, Angew. Chem. Int. Ed. 44 (2005) 4670.
[90] D.J. Collins, H.-C. Zhou, J. Mater. Chem. 17 (2007) 3154.
[91] G. Ferey, M. Latroche, C. Serre, F. Millange, T. Loiseau, A. Percheron-Guegan, Chem. Commun. (2003) 2976.
[92] D.N. Dybtse, H. Chun, S.H. Yoon, D. Kim, K. Kim, J. Am. Chem. Soc. 126 (2004) 32.
[93] Y.G. Lee, H.R. Moon, Y.E. Cheon, M.P. Suh, submitted for publication.
[94] C. Joachim, S. Roth, Atomic and Molecular Wires, Kluwer Academic, Dordrecht, 1997.
[95] T. Hertzsch, F. Budde, E. Weber, J. Hulliger, Angew. Chem. Int. Ed. 41 (2002) 2282.
[96] B.H. Hong, S.C. Bae, C.-W. Lee, S. Jeong, K.S. Kim, Science 294 (2001) 348.
[97] R. Kitaura, S. Kitagawa, Y. Kubora, T.C. Kobayashi, K. Kindo, Y. Mita, A. Matsuo, M. Kobayashi, H.-C. Chang, T.C. Ozawa, M. Suzuki, M. Sakata, Science 298 (2002) 2358.
[98] S. Takamizawa, E. Nakata, T. Saito, Angew. Chem. Int. Ed. 43 (2004) 1368.
[99] R. Matsuda, R. Kitaura, S. Kitagawa, Y. Kubota, R.V. Belosludov, T.C. Kobayashi, H. Sakamoto, T. Chiba, M. Takata, Y. Kawazoe, Y. Mita, Nature 436 (2005) 238.
[100] B.M. Krasovitskii, B.M. Bolotin, Organic Luminescent Materials, VCH, Weinheim, 1988.
[101] B.D. Chandler, A.P. Coté, D.T. Cramb, G.K.H. Shimizu, Chem. Mater. 19 (2007) 4467.
[102] J. Tao, M.L. Tong, J.X. Shi, X.M. Chen, S.W. Ng, Chem. Commun. (2000) 2043.
[103] J. Tao, J.X. Shi, M.L. Tong, X.X. Zhang, X.M. Chen, Inorg. Chem. 40 (2001) 6328.
[104] W. Chen, J.Y. Wang, C. Chen, Q. Yen, H.M. Yuan, J.S. Chen, S.N. Wang, Inorg. Chem. 42 (2003) 944.
[105] T.M. Reineke, M. Eddaoudi, M. Fehr, D. Kelley, O.M. Yaghi, J. Am. Chem. Soc. 121 (1999) 1651.
[106] B.D. Chandler, A.P. Coté, D.T. Cramb, J.M. Hill, G.K.H. Shimizu, Chem. Commun. (2002) 1900.
[107] K.-L. Wong, G.-L. Law, Y.-Y. Yang, W.-T. Wong, Adv. Mater. 18 (2006) 1051.
[108] M. Kawano, M. Fujita, Coord. Chem. Rev. 251 (2007) 2592.